A Project Report

On

Development of Microfluidic Sensor

BY

Shika Rao

2019A3PS1237H

Under the supervision of

Prof. Sanket Goel

SUBMITTED IN PARTIAL FULLFILLMENT OF THE REQUIREMENTS OF

Design Projects (ECE F366 (F367) / EEE F366 (F367) / INSTR F376 (F367)

BIRLA INSTITUTE OF TECHNOLOGY AND SCIENCE PILANI

HYDERABAD CAMPUS

(October 2021)

ACKNOWLEDGMENTS

Birla Institute of Technology and Science-Pilani,

Hyderabad Campus

Certificate

This is to certify that the project report entitled "**Development of Microfluidic Sensor"** submitted by Ms. Shika Rao (ID No. 2019A3PS1237H) in partial fulfillment of the requirements of the course Design Projects (ECE F366 (F367) / EEE F366 (F367) / INSTR F376 (F367), embodies the work done by her under my supervision and guidance.

Date: 7-12-21   **(Prof. Sanket Goel)**

BITS- Pilani, Hyderabad Campus

ABSTRACT

This project aims to contribute to medical research on Urinary Tract Infections (UTIs) using a microfluidic sensor and deep learning. A microfluidic biosensor for nitrite detection in urine is designed using Creo Parametric software and the physics is simulated using COMSOL Multiphysics software, as the presence of nitrite in urine indicates Bacterial Urinary Tract Infections. To classify other UTIs, microscopic analysis is conventionally done. Thus, microscopic images containing various urine sediments are collected and Deep Learning model YOLOv3 is used to automate the detection and classification of the urine sediments. This report also presents a thorough study of various projects carried out in this field towards a similar aim as our project, providing information on the current state of the art.

The report finally concludes by giving the results of the study and suggesting courses for future improvement of the models and for further research.

Index terms:
Microfluidic sensor, Biosensor, Urinary Tract Infections, Deep Learning, Urine sediment

CONTENTS

INTRODUCTION

Urinary tract infections (UTIs) are common and it is among the most prevalent bacterial diseases, affecting more than 150 million individuals globally each year. UTIs are majorly incident in children, elderly men, and women across all ages. Regular recurrences, Clostridium difficile colitis, renal injury in young infants, premature birth, pyelonephritis with sepsis, and complications from frequent antimicrobial usage, such as high-level antibiotic resistance[11], are all serious consequences.

Many Urinary Tract Disorders can be discovered early on by looking for compounds in the urine that aren't ordinarily present.The presence of specific molecules, such as glucose, protein, red blood cells, crystals, nitrite, and others, can be measured to indicate several diseases.

Complete urinalysis in the medical field involves the following 3 distinct testing phases as described in [9]:

1. **Visual Examination**:

Depends on the color and clarity of the urine.

2. **Chemical Examination**:

- *Dipstick Test***:**

The dipstick test for urinalysis [19] is a simple Point Of Care (POC) test for evaluating nitrite (presence of nitrite in urine indicates the presence of nitrate-reducing bacteria) and leukocyte esterase (made by white blood cells). It has been widely used since the 1980s. Nitrite, leukocyte esterase, specific gravity (urine concentration), bilirubin, pH, urobilinogen, protein, ketones, glucose, and blood (haemoglobin and myoglobin) are all assessed using this test. Each of these provide valuable information about health. This test can often be read in as little as 60 to 120 seconds and matching the color on the dipstick strip to the instructions manual would give the results of the test.

A positive result for leukocyte esterase and nitrite indicates a bacterial Urinary Tract Infection (UTI). Most of the time, if the leukocyte esterase test is positive, the nitrite is also positive.

- *Urine Culture Test:*

A urine culture test is required to determine the type of bacterial UTI. The results of this test currently range from 24 - 72 hours. Further research and technological advance is ongoing to reduce the time taken for this test.

A person may be treated without need for a urine culture only in cases wherein a person has a lower urinary tract infection which is uncomplicated.

Escherichia coli (E. coli) is the bacteria predominantly responsible for bacterial UTIs.

3. **Microscopic Examination**:
This test is done only by prescription of a doctor or if the results of the chemical and visual examination are abnormal.
The purpose is to examine urine sediment to identify and count the casts, crystals, type of cells, and other sediments like mucus and bacteria.

Sediment	Effect
Erythrocyte	Glomerular hemorrhage
Leukocyte	Urinary system inflammation
Epithelial	Lesions in different parts
Squamous epithelial cells	Bacterial urethra disease
Low transitional epithelium	Renal tubule damage
Cell cast	Acute glomerulonephritis
Waxy cast	Renal tubular necrosis
Granule cast	Nephrotic syndrome
Adipose cast	Tubular injury
Wide cast	Renal failure
Transparent cast	Chronic glomerulonephritis
Calcium phosphate crystal	Hyperparathyroidism
Calcium oxalate crystal	Kidney or bladder stones
Magnesium ammonium phosphate crystal	Bladder stones
Uric acid crystal	Gout
Lactobacillus	Urethral inflammation

Source: [27]

Introduction to colorimetric analysis and microfluidic sensors for nitrite detection

Since dipstick tests are suited for everyday monitoring of personal health concerns in the home, the urinalysis chemical testing system can also be used for home diagnosis. Though the dipstick test has shown to be effective, it does have some drawbacks, such as sensitivity and accuracy [14].

Furthermore, users must follow the commercial strips step by step; additionally, home users must analyse the phenomenon on the strips according to the user manual. As noted out in [3,] many home users are perplexed by strip testing.

The major limitation of the dipstick test is that a quantitative measure of the nitrate content in urine is not provided.The urine nitrite dipstick assays are qualitative, and any detectable nitrite is assumed to suggest infection of the urinary tract. This emphasises the necessity of the dipstick's limiting sensitivity. As the concentration of urine nitrite approaches the detection limit, the user must decide if the dipstick has turned a very light pink. Thus, when minor changes in the concentration are tested by dipstick techniques, there is significant heterogeneity across technologists, resulting in incorrect results, as illustrated in [10, 1978].

Hence, there arises a need for quantitative and qualitative, automatic detection of nitrite.

In [13], nitrite detection methods like chemiluminescence, spectrofluorometric, and spectrophotometric methods have been compared and contrasted based on their benefits and limitations. Spectrofluorometric and chemiluminescence procedures offer a higher limit of detection than spectrophotometry, although they are more expensive.

The Griess assay [13] is a well-known and well-established spectrophotometric detection method for nitrite detection. In a microfluidic environment, the Griess test is performed by combining the reagent with a sample present in microchannels. Small amounts of reactant solutions can be used thanks to the embedded microchannels, which have a great surface-to-volume ratio, efficiency, and reproducibility. In addition, microchannel streams typically create laminar flow, allowing for precise control of time and reaction conditions.

Thus, in this project, the spectrophotometric colorimetric detection method for nitrite is adopted using the Griess test in a microfluidic environment. The modeling and simulation of this sensor is done using COMSOL multiphysics software.

Introduction to deep learning applied to microscopic images of urine sediment

A qualified medical laboratory technologist is required to classify urine sediment using the urinalysis microscopic examination system. The sediment type is important in clinical diagnosis of UTIs as it is possible to determine the disease by distinguishing the amount (quantitative analysis) and type of sediment (qualitative analysis) in a urine specimen. RBCs and WBCs make up the majority of the higher clinical value of urine sediment. The quantitative and qualitative measurement of WBCs and RBCs in urine sediment can also aid in the exploration of different treatment options for urethral disorders. Nephrologists began to express worry in 2005 about the frequent differences in some urine sediment microscopy results [22]. For example, based on reports from medical technologists and nephrologists, the diagnostic accuracy rates for acute renal injury were 25% and 69–92%, respectively [22]. Thus, there is substantial variability among technologists and medical practitioners due to the subjective nature of interpretation of the urine sediment, thus leading to inaccurate diagnosis.

Dysmorphic red blood cells (RBCs) are often misclassified as WBCs due to their similarity in terms of cellular morphology as seen in Fig 1. In addition, dysmorphic RBCs often occur in urine sediment as they are usually transformed due to squeezing through blood vessels walls. Thus, the detection accuracy significantly declines when there is the presence of many dysmorphic RBCs in urinary sediment.

Hence there arises a need for quantitative and qualitative, automatic analysis of urine sediment.
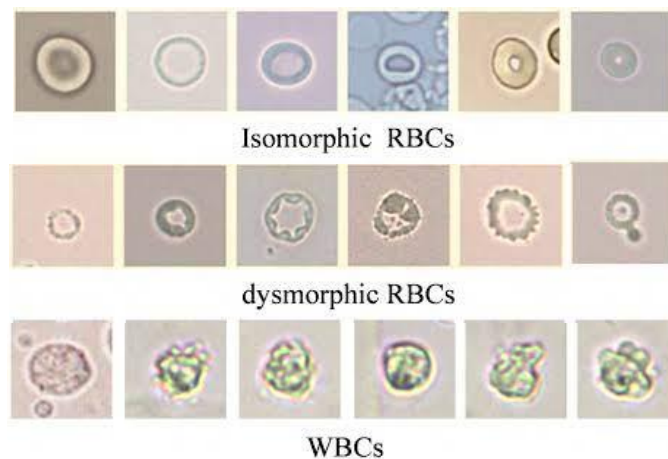
(Fig 1. Isomorphic and Dysmorphic RBCs and WBCs. (From [23])

Several computer vision-based techniques for urine sediment microscopy have been proposed in various research. However, due to cellular heterogeneity, this is still a difficult task. Object detection and classification based Convolutional Neural Networks are applied to microscopic urine sediment images. Semantic segmentation networks, though popular for biomedical imaging purposes, would not be necessary here as detailed information for each sediment particle in the urine would not be required as long as it is identified accurately.

Thus, in this project, transfer learning using pre-existing object detection based Convolutional Neural Networks is adopted to detect and classify urine sediment. This is done using Python and Google Colaboratory.

In this project, we deal with Urinary Tract Infections specifically. In [2], [9], and [10], it was pointed out that nitrite detection is the most common test for bacterial UTI detection in urine samples. Thus, in this project, a microfluidic sensor is designed for the automatic quantitative detection of nitrite in urine samples to indicate a bacterial UTI. As seen above, if the UTI is not bacterial in nature or if there is some abnormality/uncertainty after the chemical tests, a microscopic examination is the next step. Thus, in this project, we also aim to use deep learning for automatic detection and classification of cells, casts, etc. in the microscopic images to identify the underlying infection/disease so that variability and error could be avoided.

The remainder of the report is organized as follows. Chapter 2 introduces the pre-existing related research in the Review of Literature. Chapter 3 shows the data preparation process and the block diagram of the overall flow of the proposed methodology. The methodology of each of the methods are discussed and the results of the same are too.

REVIEW OF LITERATURE

Colorimetric analysis and/or MEMS sensors for nitrite detection

In one of the first studies toward building microfluidic sensors employing colorimetric sensing, Griess reagent was used to carry out the reaction with a sample on a glass microfluidic device in [15]. The authors used Griess reagent to construct a microfluidic sensor for colorimetric detection of nitrite using polymethyl methacrylate (PMMA). The authors of [18] described a three-layered microfluidic system for nitrate detection in mineral water using the Griess test for colorimetric analysis.

In [7, 2010], the authors utilised thread as a matrix for the creation of diagnostic test systems. It was examined for nitrite, glucose in artificial urine, and other contaminants. The response times were comparable to a standard dipstick. The response times were similar to those of a conventional dipstick. The quantification of nitrite was not addressed in this paper.

An opinion was offered in [8, 2011] on biosensors for UTI diagnosis, antimicrobial susceptibility testing (AST), and pathogen identification. Blood glucose sensor and pregnancy test kits were compared with existing UTI biosensors and microfluidics to indicate the future scope in research required to improve the accessibility of UTI biosensors.

Laboratories have developed and widely accepted automated urine flow cytometry systems which can detect bacteria, WBCs, RBCs, epithelial cells, crystals, casts, and yeasts [20], [21]. These technologies, however, do not provide diagnostic or susceptibility information.

UTI Sensor Array [31], [32], [33], [34] is a biosensor for the identification of bacteriuria. The sensor involves an array of electrochemical sensors with DNA probes that serve as bacterial recognition elements.

In [6, 2019], a Microfluidic Lab-on-a-Chip (LOC) Device was designed for photocolorimetric detection of nitrite, nitrate, and pH values in water samples. To isolate nitrite, the authors used a reaction with sulfanilic acid and Beta-naphthol. The microchannel system was designed using COMSOL multiphysics and the pressure, flow rate and reagents concentration distribution was simulated. The paper portrayed the modeling of the lab-chips using COMSOL, but the overall proposed automatic computerized system was not tested though previous research was identified and cited to prove the feasibility of the same.

A portable microfluidic device for integrated detection and quantification of nitrite was designed in [5, 2019]. A COMSOL multiphysics simulation was created first, and the microfluidic device was modelled accordingly. A regulated Griess assay reaction based experiment was carried out in a polydimethylsiloxane (PDMS) microfluidic chip. A syringe pump was designed to inject the sample and reagent. Most of the parts were made via 3D printing. The LED and photodiode were used for photometric detection. To obtain magnified photodiode output with reduced noise, a transimpedance amplifier circuit was constructed. A microprocessor and an Android application to

control and store the data was used to integrate the entire system. Bluetooth connectivity was used for communication between the application and the microcontroller. It was spectrophotometrically validated and a calibration equation was created to relate the voltage output of the device to the absorption.

An LED and photodiode (peak response of the diode at the wavelength where the chromophore exhibited absorption) were used to design a portable and autonomous system for real-time colorimetric detection in [4, 2021]. The spectrophotometric measurement of nitrite was done with Griess Reagent, and the colorimetric detection of phosphate was done with the molybdenum blue method. It has Bluetooth modules and Internet of Things (IoT) for data transmission both offline and online. This equipment was used to evaluate soil samples, and the results were confirmed using a UV–vis spectrophotometer. This study did not include the development of a MEMS/microfluidics based sensor.

Deep Learning or Image Processing for Urine Sediment Detection and Classification

In [26, 2017] the automation of microscopic urine sediment analysis in digital images to find cystine crystals was implemented. Image processing by segmentation, localization, Canny Edge Detection, and Probabilistic Hough Transform was carried out. An algorithm was designed to automatically detect hexagonal cystine structures and it facilitated detection of multiple cystine crystals in the same microscopic image.

In [23, 2018], Faster Region based Convolutional Neural Network (Faster R-CNN) was implemented for design of a microscopic urinalysis system. A dataset of 6,000 urinary sediment images with 2 classes namely, RBCs and WBCs was collected and annotated. Isomorphic RBCs, dysmorphic RBCs and WBCs were identified successfully. However, other types of urinary sediments like epithelial cells, crystals, and cysts were not included as part of this study.

In [24, 2018], a Feature Pyramid Network with the DenseNet backbone (DFPN) model was proposed to decrease class confusion in the microscopic images of urine sediment. Faster-RCNN and FPN were integrated to form the basic model. Attention module and a Class-Specific Attention module was added. Then, the DenseNet backbone network was used over the baseline model of FPN on ResNet. High levels and multiple levels of semantic segmentation were obtained. In [30, 2018], the dataset from [24, 2018] was used to analyse the performance of Faster RCNN and Single Shot Multibox Detector (SSD) for object detection.

In [28, 2019], two categorization approaches were compared: a heuristic model based on the combination of WBC and bacterial count, and machine learning based on 3 algorithms: Neural Networks, Random Forest, and Extreme Gradient Boosting. In the diagnostic lab of Severn Pathology in Bristol, the heuristic approach has been successfully deployed in clinical practise.

In [29, 2019], the a network combining AlexNet network and Area Feature Algorithm (AFA) was designed for urine sediment analysis. 3 CNN models were combined with the AFA modules to solve the 'weakening cell area feature' defect of CNNs. Transfer learning was performed to train the network and data augmentation was performed to inflate the dataset in order to improve the accuracy of the model.

In [27, 2020], seven biological components were utilised as detection targets in microscopic imaging of urine: leukocytes, erythrocytes, epithelial, low-transitional epithelium, squamous epithelial cells, crystal, and casts. The basic RetinaNet model's Resnet50 backbone and feature pyramid net (FPN) were employed for feature extraction and detection, classification, and localization. The impact of anchor scales and various weight initialization techniques on the model's performance was studied.

METHODOLOGY

Functional Block Diagram:

The proposed methodology's overall flow is depicted in Figure 2 below. The flowchart highlights some of the methodology's important decision points in a visual format. This methodology's modular design makes it simple to anticipate future modifications in functionality and flow to improve efficiency and integrate with other additional approaches.
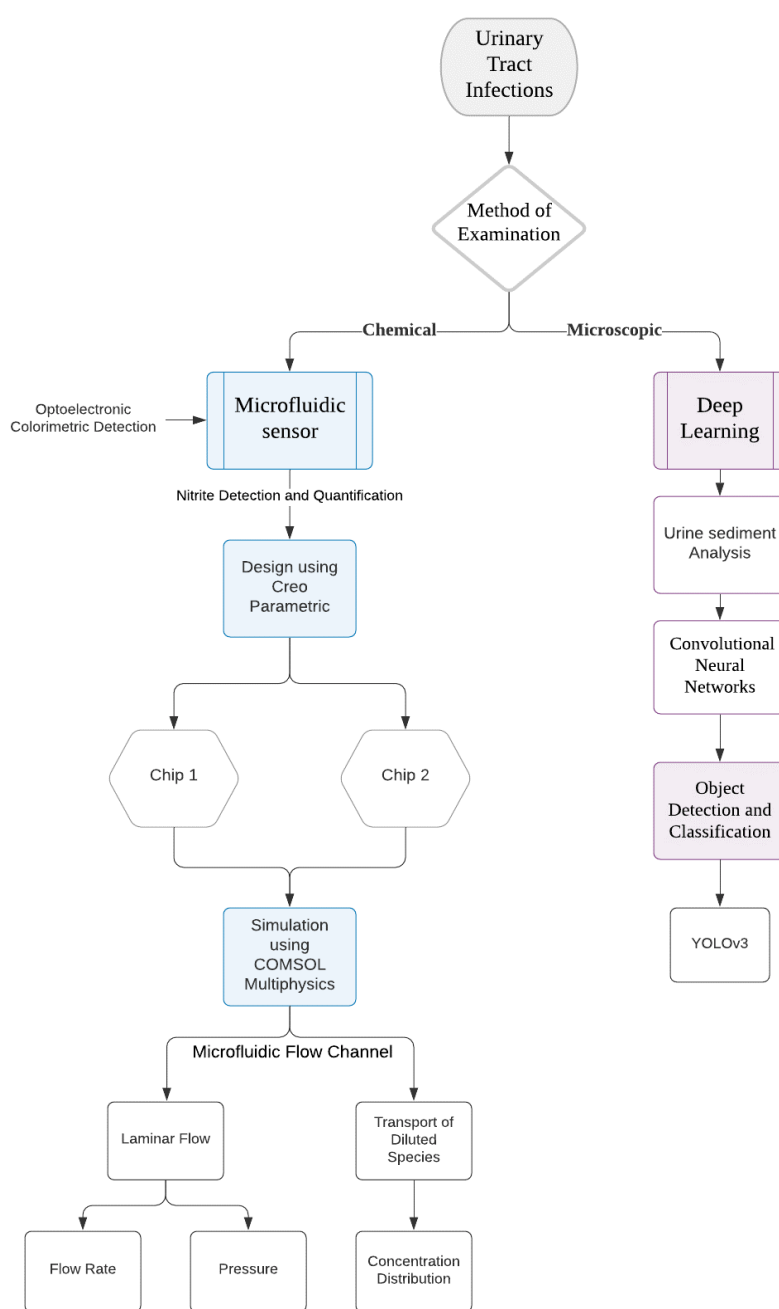
(Fig 2. Flowchart of Methodology)

PART 1-

Microfluidic sensor for detection of nitrite

Two chips were designed and simulated using Creo Parametric and COMSOL Multiphysics respectively.

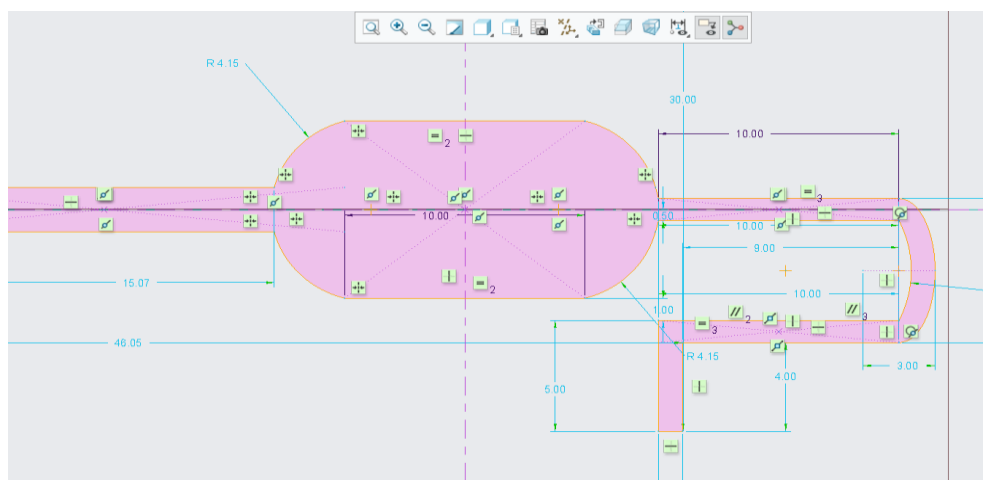### *Creo Parametric design:*

The flow channels for the microfluidic chips were designed using Creo Parametric 6.0.2.0 Student Edition (PTC Inc.) as shown below. The width of the channel for both chips is 4cm and length is almost 8cm. The thickness is 5mm.

Chip1:

A +45° Y microchannel was designed due to the advantages in [41], [42].
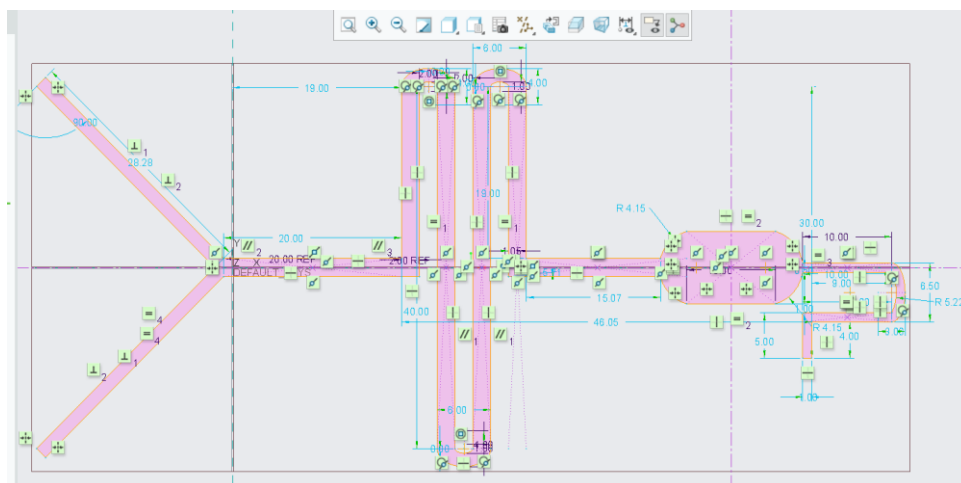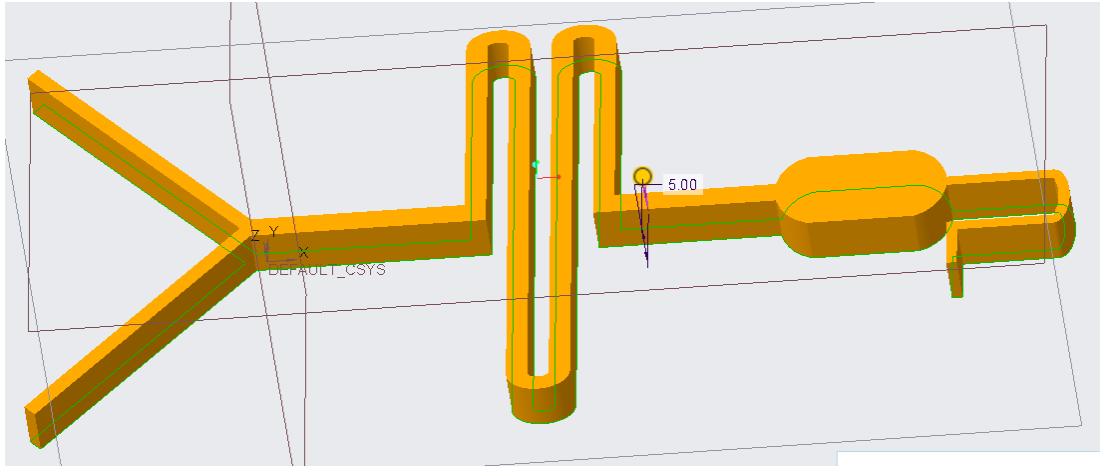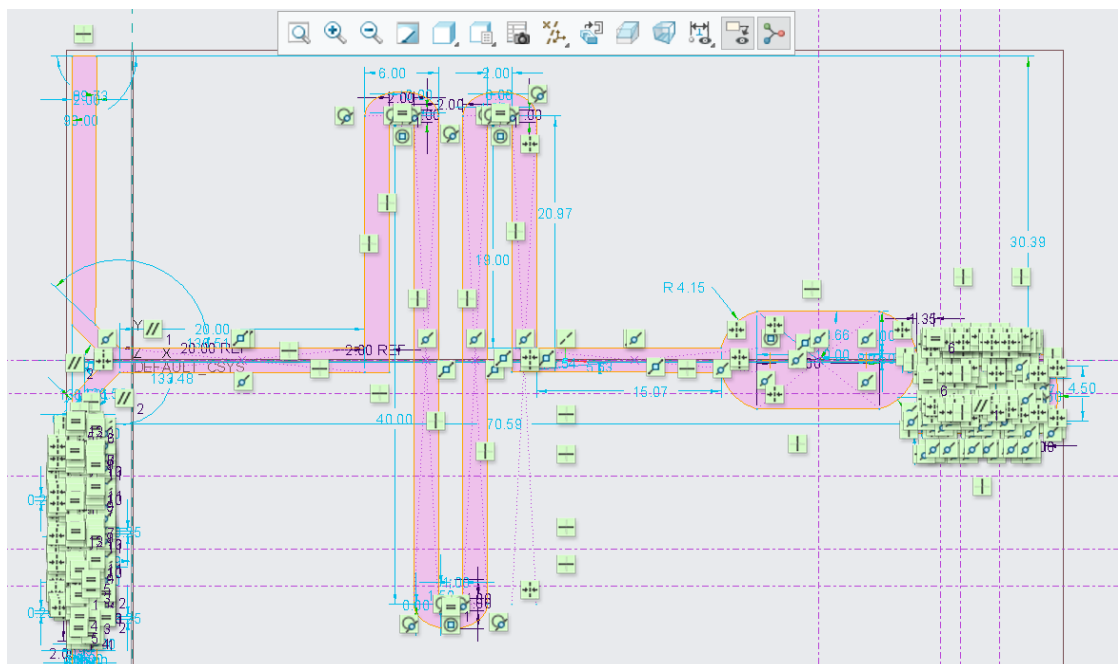

(a)

(b)

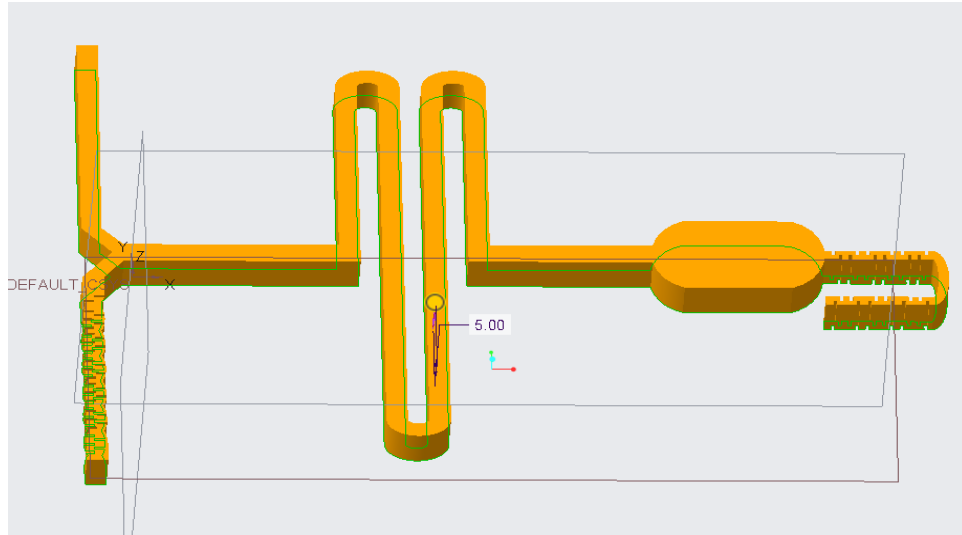(Fig 3. 2D representation of the microfluidic sensor)

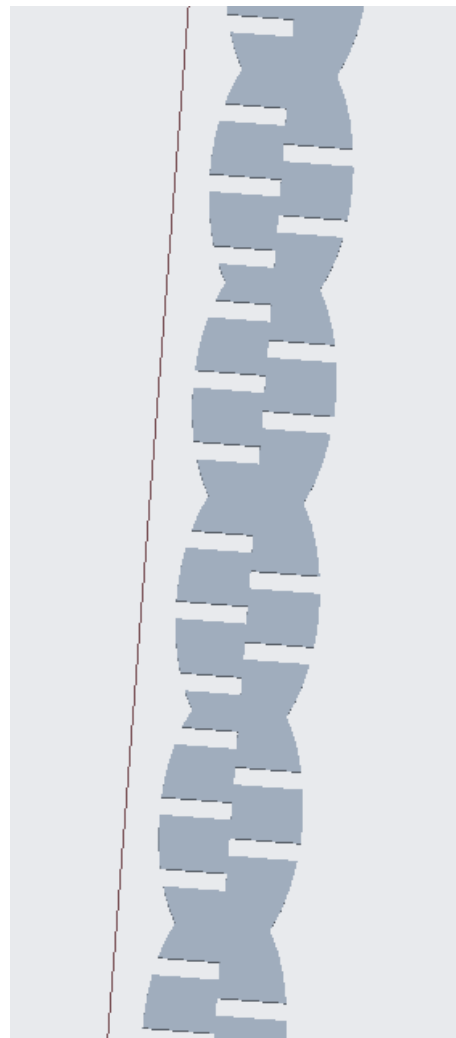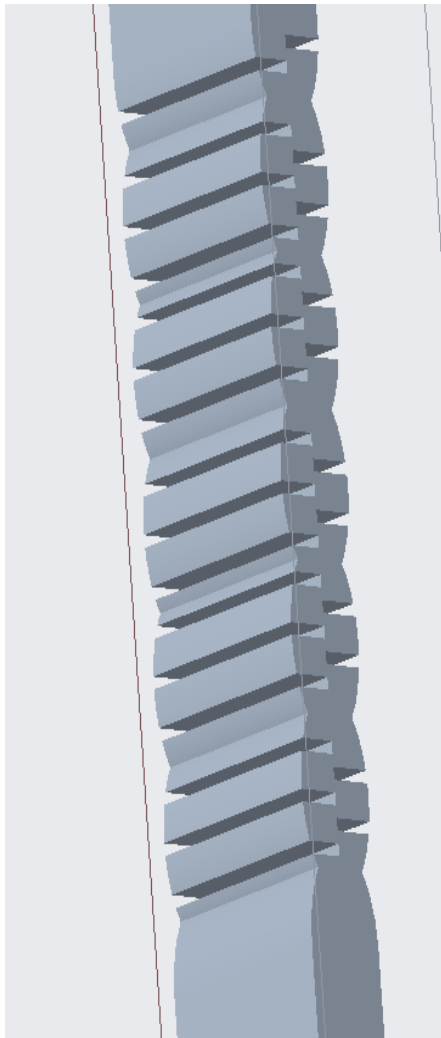(Fig 4. 3D representation of the microfluidic sensor)

Chip2:

In flow channel 2, inter-digitized orthogonal obstacles were added to the design for the dual purpose of- a mixing channel for better concentration combination due to augmentation of inlet and outlet in the flow channel, and to slow down the flow of urine in the augmented inlet as adopted in [43]. The elliptical augmented inlet was used in the design as per [44].

(Fig 5. 2D representation of the microfluidic sensor)

(a)

(b)

(Fig 6. 3D representation of the microfluidic sensor and the interdigitized orthogonal obstacles)

COMSOL simulation:

COMSOL Multiphysics 5.6 was used to simulate the designed microfluidic flow channels. Laminar Flow (spf) physics and Transport of Diluted Species (tds) physics were coupled for the analysis. A 3D model was simulated. Creo Parametric LiveLink was used to import the designed .prt files to the COMSOL interface and the microfluidics module was used for simulation of tds physics.

Laminar flow for single phase fluid flow is characterised by the Navier-Stokes equation with the equation:

- the continuity equation:

$$\rho \nabla \cdot u = 0$$

and the momentum equations:

$$\rho \frac{\partial u}{\partial t} + \rho(u \cdot \nabla)u = \nabla \cdot [-pI + \mu(\nabla u + (\nabla u)^T)] + F$$

The nature of the fluid flow is determined using the Reynolds number (dimensionless). It is the ratio of inertial to viscous force, i.e.

$$\mathcal{R} = Reynolds\ number$$
$$= \frac{Inertial\ force}{Viscous\ force}$$
$$= \frac{\rho u \ell}{\mu}$$

where u represents fluid flow speed, μ denotes fluid dynamic viscosity, ρ indicates fluid density, ℓ represents the channel length for the fluid. The existence of turbulent flow is indicated by a high $\mathcal{R}$ value, whereas the presence of laminar flow is indicated by a low $\mathcal{R}$ value. We use these parameters (ρ, μ, ℓ and u) in our proposed models so that $\mathcal{R}$ is less than 2000 and laminar flow for miscible fluids is applicable [45].

Transport of diluted species (concentration fields), based on Fick's law of diffusion, was used to model 'mass transfer by diffusion and convection'. The mass balance equation includes chemical reactions:

18

$$\rho \frac{dV}{dt} + \rho (V.\nabla) V = -\nabla p + \mu \nabla^2 V$$

$$\frac{dc}{dt} + (V.\nabla) c = D \nabla^2 c$$

where ρ is density of fluid, V is the fluid velocity vector, μ denotes dynamic viscosity, c is the concentration constant, p is pressure exerted, and D represents the diffusion coefficient.

This interface provides a predefined simulation environment for studying the chemical species transport via diffusion and convection mechanisms. This interface considers that all species are dilute, with low concentrations in comparison to a solvent fluid.

The species flux across a boundary can be specified by the fluid flow. The total flux of a species, ci, is calculated as follows:

$$-D_i \cdot \nabla c_i + u c_i = N_i$$

where: Ri indicates reaction rate in mol/(m3·s) and Ni indicates the user-defined flux (mol/(m2·s)).

The material properties used during the simulation are:

Property	Variable	Value	Unit	Property group
✓ Density	rho	1005	kg/m³	Basic
✓ Dynamic viscosity	mu	0.00109	Pa·s	Basic

That is because the density of urine ranges from 1002 to 1030 kg/m^3 with healthy urine density at about 1005 kg/m^3. The dynamic viscosity of urine is close to water at 1.09 cP.

The parameters of the simulation for chip 1 are as follows:

▼ Parameters

Name	Expression	Value	Description
uo	1 [mm/s]	0.001 m/s	Inlet Velocity
cL	1 [mol/m^3]	1 mol/m³	Left Inlet Concentration
D	1e-11 [m^2/s]	1E-11 m²/s	Diffusion Constant
t	0 [s]	0 s	Start time
cR	2 [mol/m^3]	2 mol/m³	Right Inlet Concentration

The parameters of the simulation for chip 2 are as follows:

Name	Expression	Value	Description
uL	1 [mm/s]	0.001 m/s	Left Inlet Velocity
cL	1 [mol/m^3]	1 mol/m³	Left Inlet Concentration
D	1e-11 [m^2/s]	1E-11 m²/s	Diffusion Constant
t	0 [s]	0 s	Start time
uR	5 [mm/s]	0.005 m/s	Right Inlet Velocity
cR	10 [mol/m^3]	10 mol/m³	Right Inlet Concentration

The concentration was taken as varying for both inlets so that the mixing characteristics could be simulated by the transport of diluted species interface.

A suitable swept mesh was chosen for simulating fluid dynamic flow. Stationary study was performed followed by a time dependent study. The stationary study was performed such that Laminar Flow physics was simulated separately as Study1 and then it was coupled using Multiphysics with Transport of Diluted Species physics as Study2. Then a time dependent study was performed for the coupled multiphysics upto 3s in intervals of 0.2s. The diffusion coefficient was taken as a varying parameter in the time dependent study so that its effect could be studied on velocity, pressure, and concentration of fluid flow.

Colorimetric Reagent:

In [2], it was proven that the Griess Nitrate assay is one of the most accurate tests for nitrite detection. The Griess reagent is 1% sulphanilamide (SA) and 0.1 % n-(1-naphthyl) ethylenediamine dihydrochloride (NED) in 5% polyphosphoric acid H3PO4. Griess reagent is used for the detection and quantification of nitro groups in many applications, including samples like urine and blood.
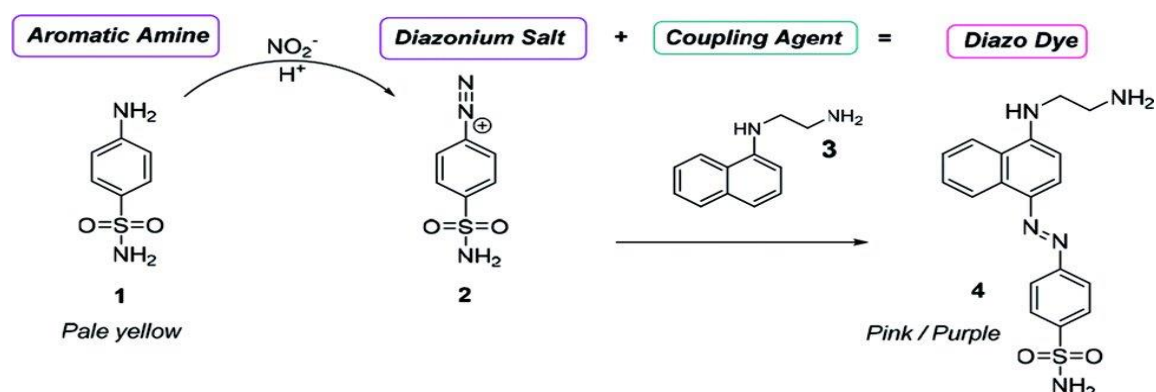
(Fig 7. Griess Reaction (From [46]))

In chip1, any of the inlets of the Y shaped microchannel can be used for injection of Griess reagent and in chip2, the inlet without the augmented rectangular digitations is for injecting Griess reagent.

Colorimetric Detection using Optoelectronic components:

Colorimetric analysis is based on the principle that a substance absorbs light at a specific wavelength while allowing light at other wavelengths to pass through unaffected. The Lambert and Beer law [47] can be used to correlate the optical absorption of colour at a wavelength to the concentration of the analyte.

The following methods can be used for the colorimetric quantitative analysis in the microfluidic device:

1. The use of optoelectronic components, such as LED and photodetectors
   - Voltmeter reading to correlate the voltage output to quantity of nitrite in analyte
   - Microcontroller and Analog to Digital Converter (ADC) to display through flexible numeric display (FND) [as in 50]
   - Microcontroller and display through Smartphone Application [as in 5]
2. Conventional UV-vis spectrophotometers which directly quantify the nitrite content

The colorimetric measurement of analytes in the two chips can involve the usage of a quasi-monochromatic light source and a photodetector as an LED and photodiode combination is small and portable. LEDs are low-cost, effective, small, economical, and field-deployable with little power requirements. These optoelectronic components with narrow emission spectra allow for selection of specific components [48]. Using an LED and photodiode could be effective for colorimetric detection of analytes such as nitrite as in [49].

A green LED was chosen because it has a high spectral sensitivity in the desired wavelength range. The Photodiode selection was made such that the photocurrent varies linearly with the irradiance.

Method Assessment:

This project only portrays the design and simulation of a microfluidic sensor. However, this chip can be integrated to make a fully functional lab on a chip device as seen in [5, 2019] and as hypothesized in [6, 2019].

RESULTS of PART 1:

Simulations for varying lengths of the flow microchannels were studied, and the final selection was made based on the results of the simulation. The results for fluidic component flow rate, pressure, and concentration distribution are examined for both of the chips below. Syringes controlled by microcontroller can be used to inject the reagent and sample into the microfluidic device to maintain the constant inlet initial flow velocity.
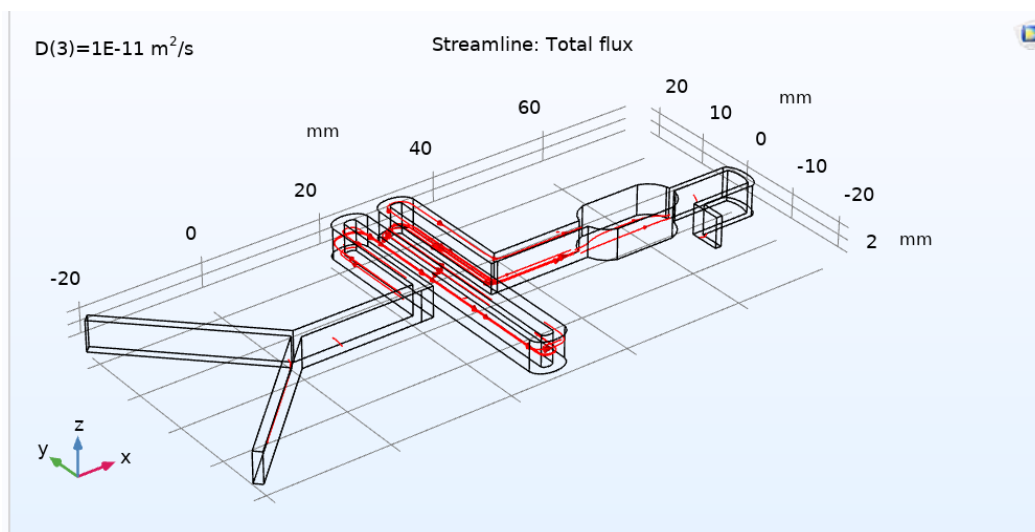
Chip1:

The simulation study time for chip 1 was about 1 hour 30 minutes.
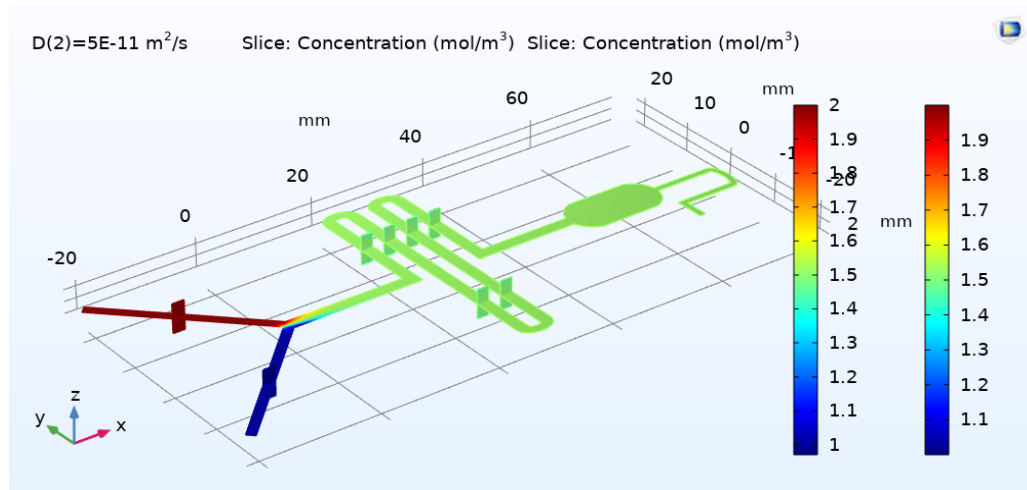
Simulation of Concentration Distribution

Different concentrations are represented by the varying hues at the inlets. The reagent and sample mixture proceeds along the flow until it reaches uniform concentration at the end of the channel.
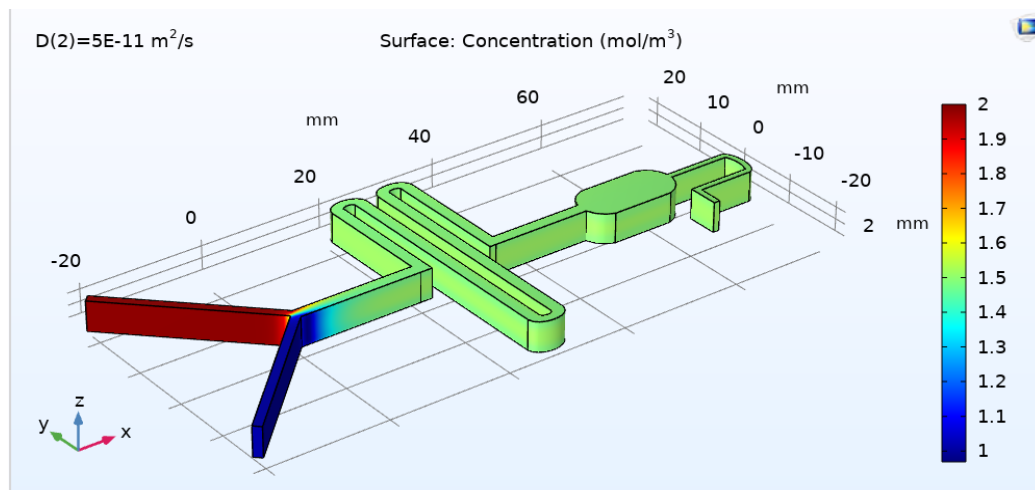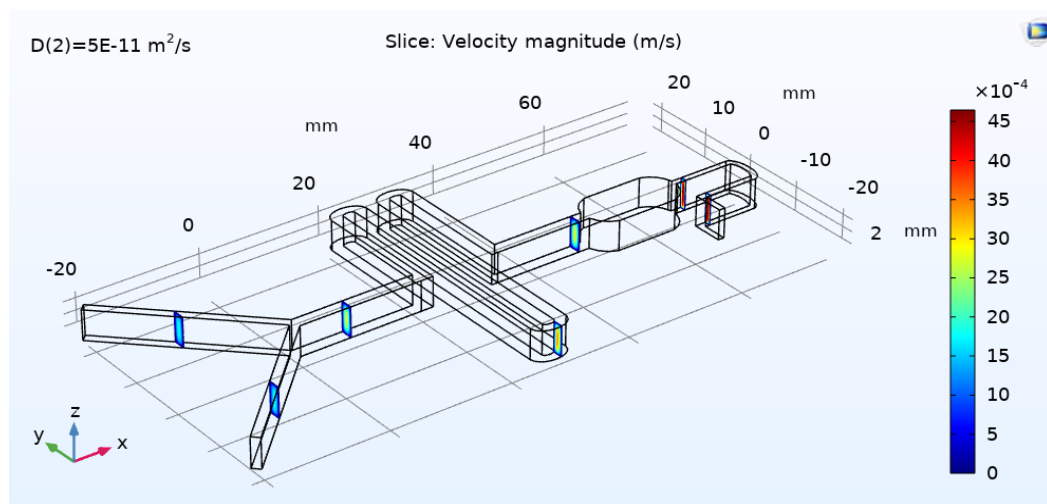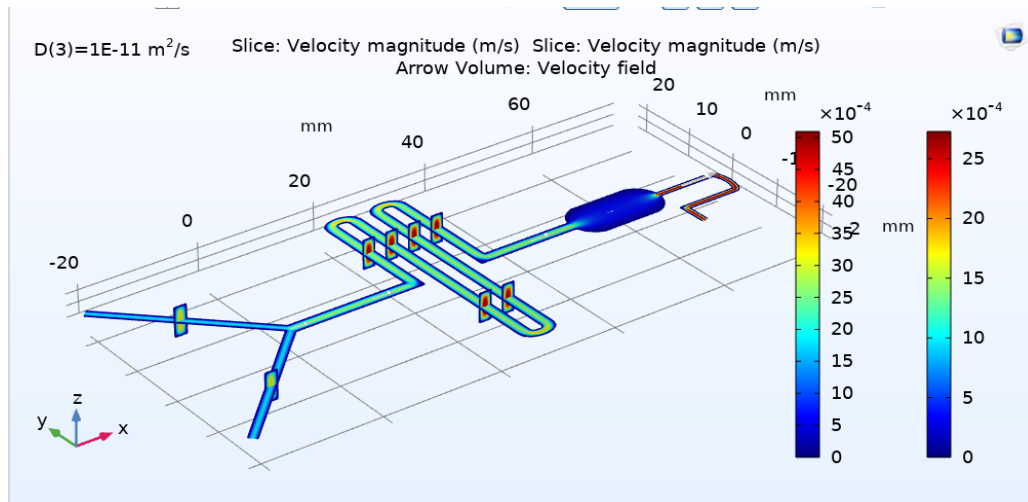

(a)

(b)

(c)

(Fig 8. Concentration Profile simulated using tds and spf coupled physics)

Velocity Profile Simulation Results

The computational simulation is used to optimize the fluidic velocity flow that could generate linear concentration gradients inside the microfluidic device.
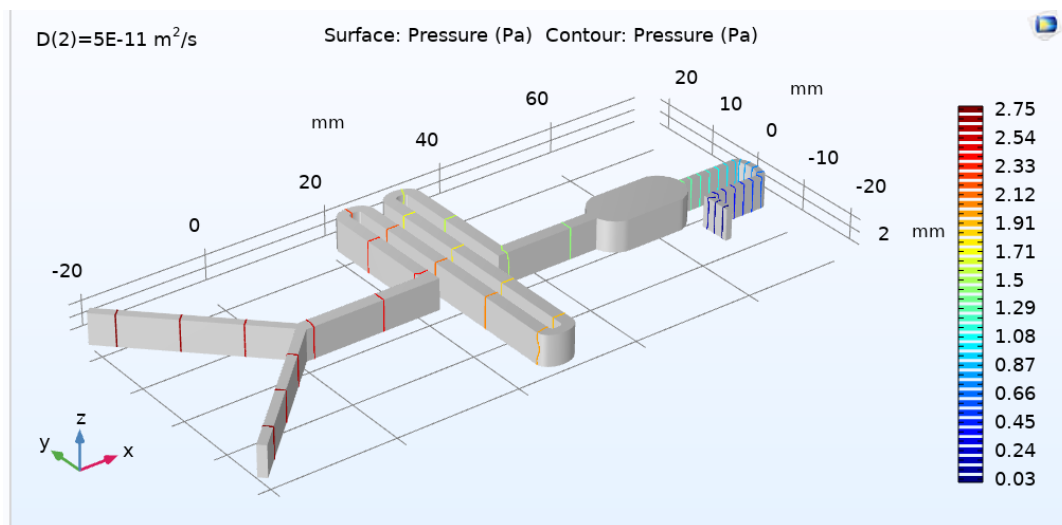

(a)

(b)

(Fig 9. Velocity profile simulated using spf physics)

Pressure profile Simulation Results

The pressure distribution results for a particular diffusion coefficient and at a particular time in the time dependent study are given in the 2 figures below respectively.

(a)

(b)

(Fig 10. Pressure profile simulated using spf physics)

Chip2:

The simulation study time for chip 2 was about 3 hours 45 minutes.

Simulation of Concentration Distribution

Varying hues show different concentrations at the inlets. The reagent and sample mixture moves down the channel, eventually reaching a uniform concentration.
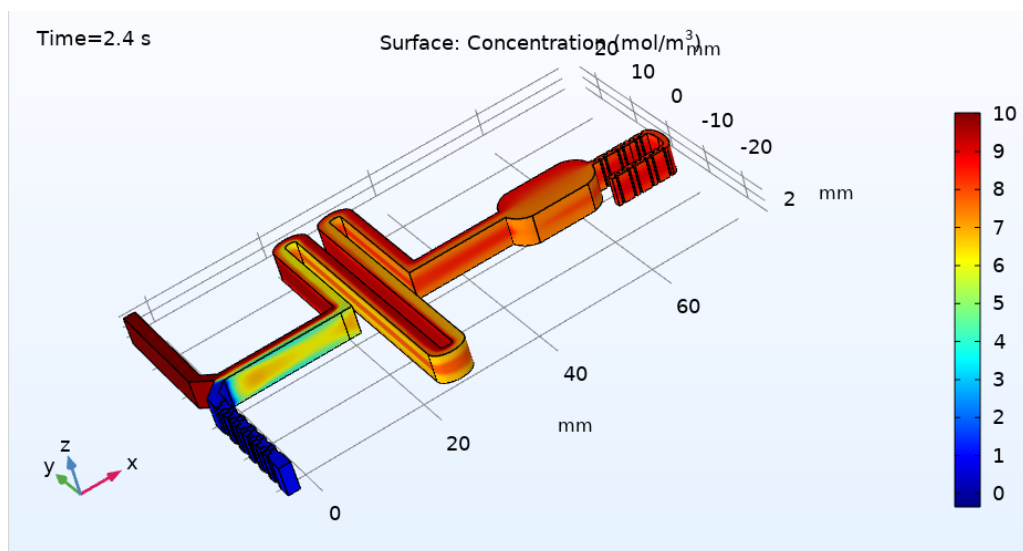
(a)
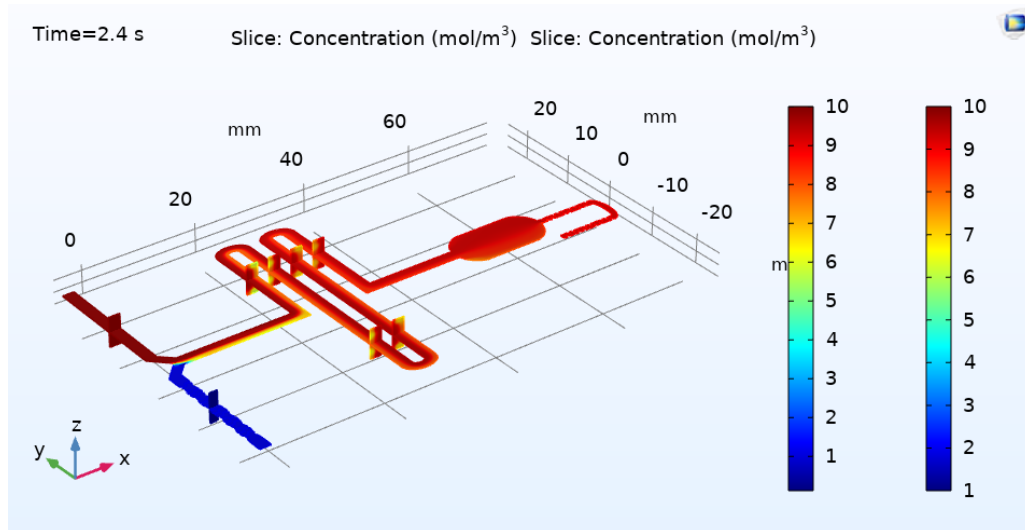
(b)
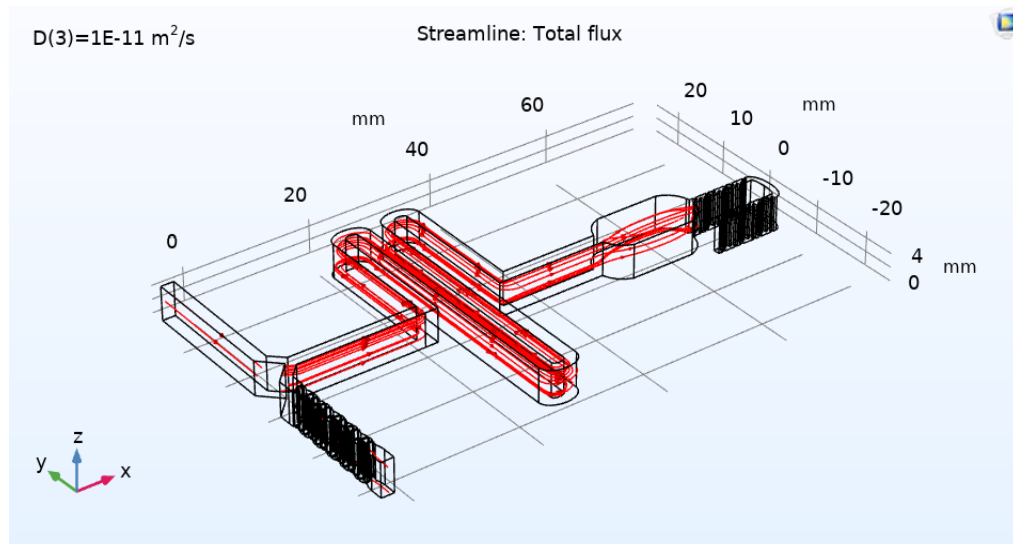
(c)

(Fig 11. Concentration Profile simulated using tds and spf coupled physics)

Velocity Profile Simulation Results

This simulation is used to calculate the optimal fluidic velocity flow that could generate linear concentration gradients in the flow channel of the microfluidic chip.
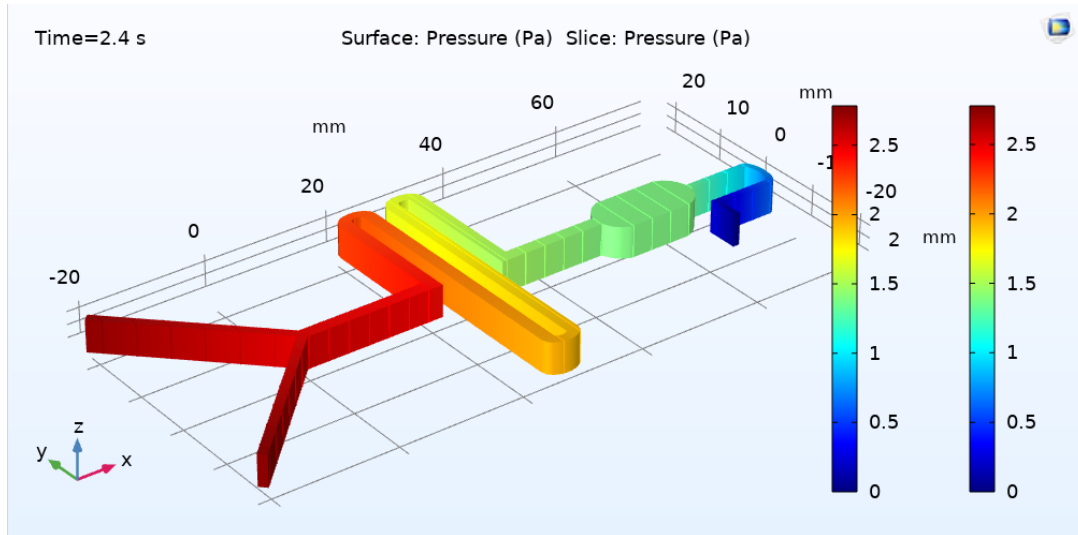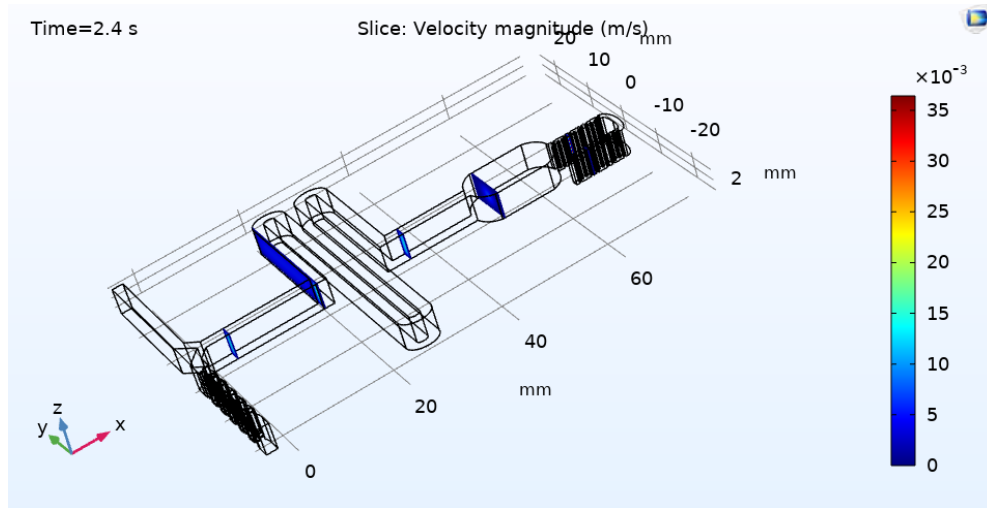
(a)
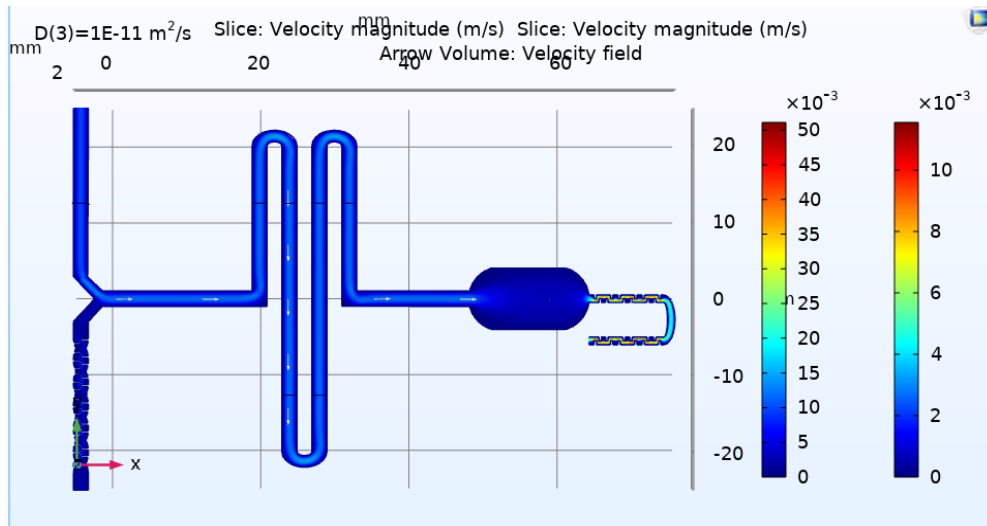
(b)
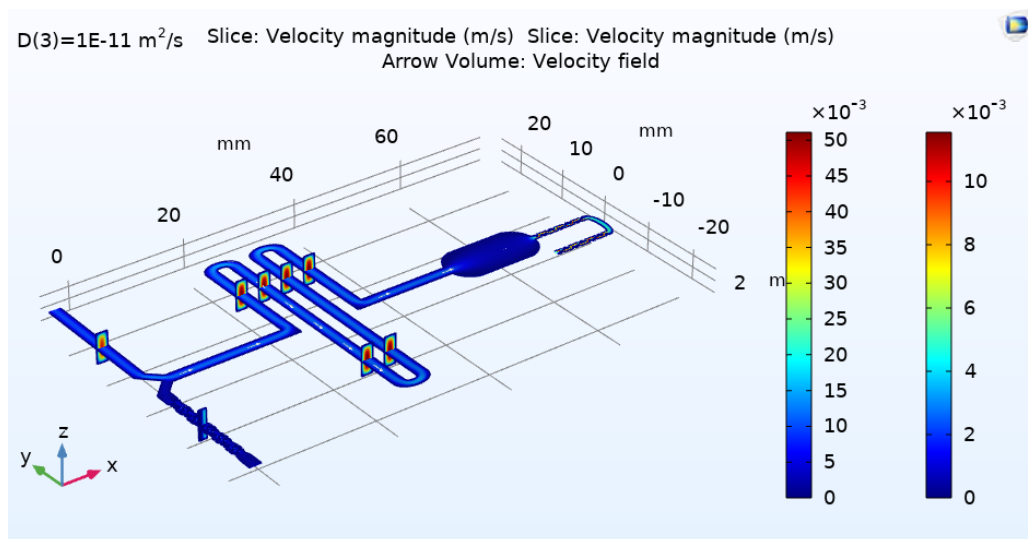
(c)

(Fig 12. Velocity Profile simulated using spf physics)

Pressure profile Simulation Results

The pressure distribution results at a particular time in the time-dependent study are given in the 2 figures below.
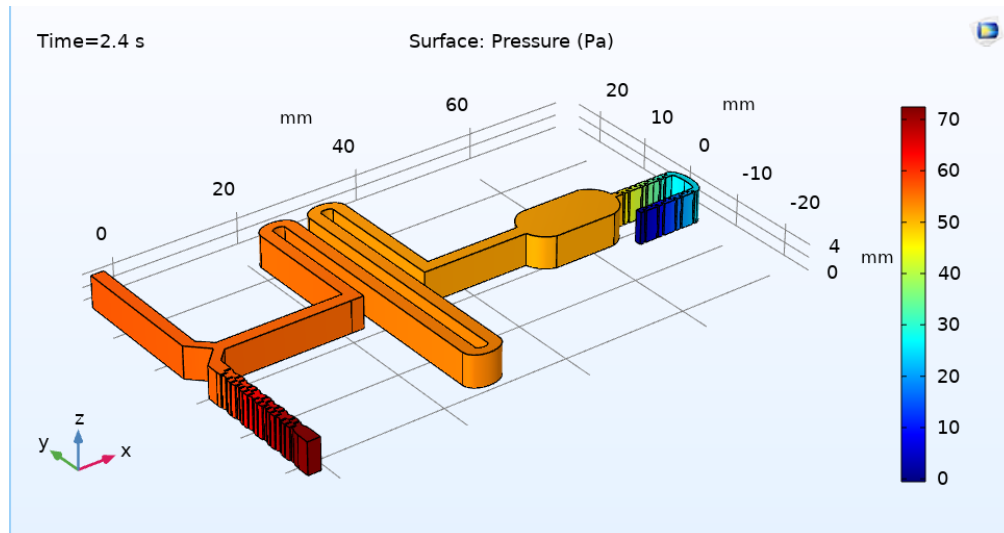
(a)
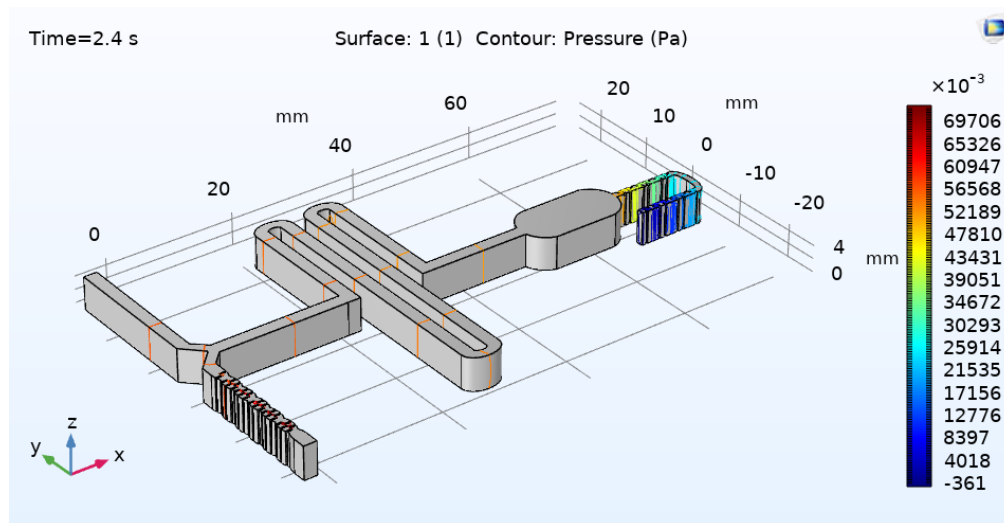
(b)

(Fig 13. Velocity Profile simulated using spf physics)

PART 2-
# Deep Learning for detection and classification of the sediment

Dataset:

The dataset publicly provided for future investigations in [24] has been used for our project. The dataset was manually annotated by qualified medical technicians.

https://github.com/174614361/Urinary-Sediment-Dataset

https://drive.google.com/drive/folders/18VqmoqK7dVSdxiyEE6qCfIpS8UOqqIBS

In the USE dataset, there are 42759 labelled instances in 5377 images. The dataset contains 7 urinary sediment categories namely leukocyte(leuko), mycete, crystals(cryst), cast, erythrocyte(eryth), epithelial(epith), and epithelial nuclei(epithn).

The dataset is divided into 4256 images for training, 852 images for validation, and 173 images for testing. For this project, 4256 images were used for training, 1019 images were used for validation, and 6 images for testing.
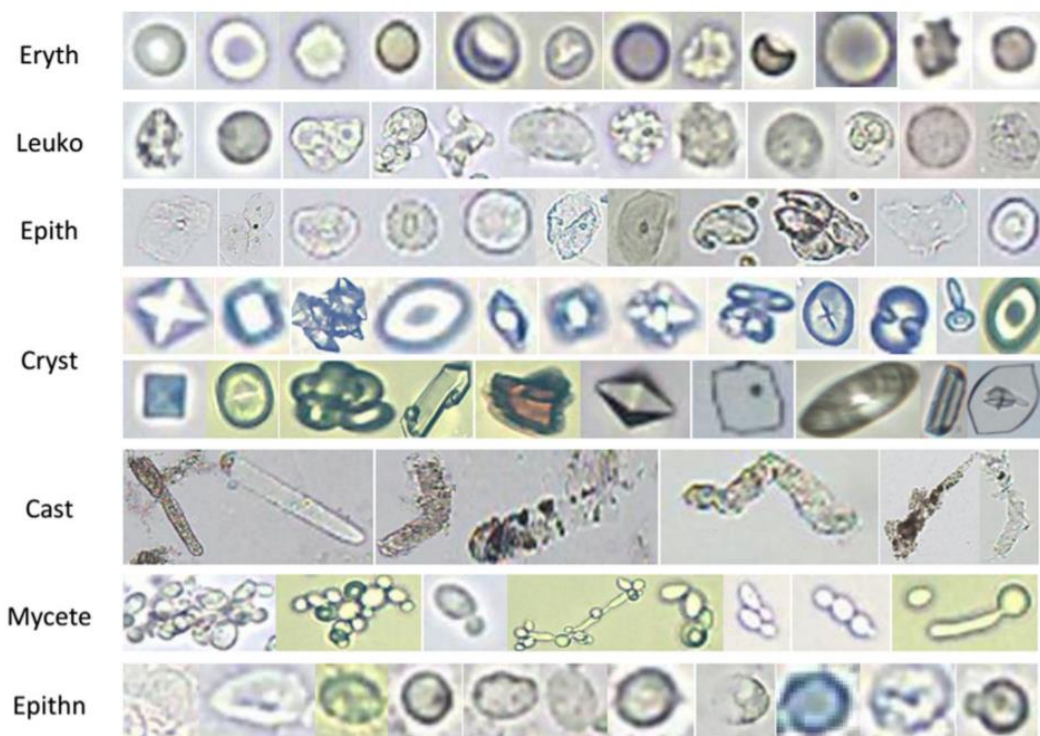
Fig. 4 Selected samples of urinary sediment particle

(Fig 14. Various classes in the USE Dataset (From [38]))

Exploratory Data Analysis:

This involves plotting the classes in the dataset for better visualization purposes.
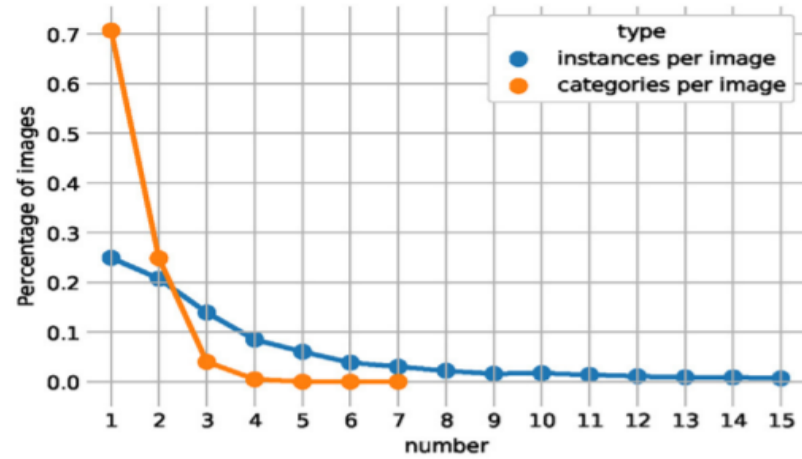
(a) (From [24])
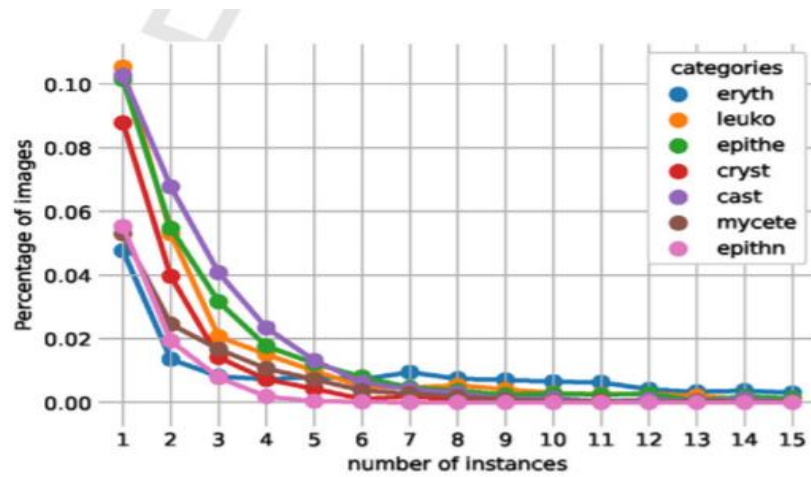
(b) (From [24]))
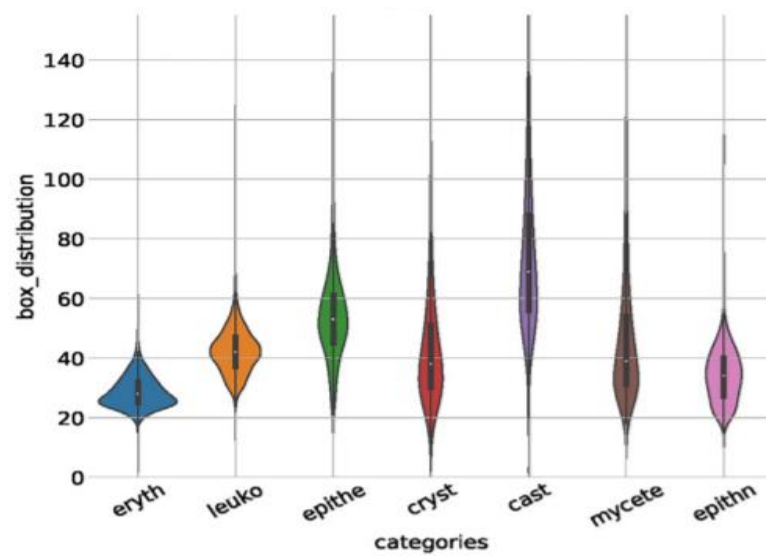
(c) (From [24]))
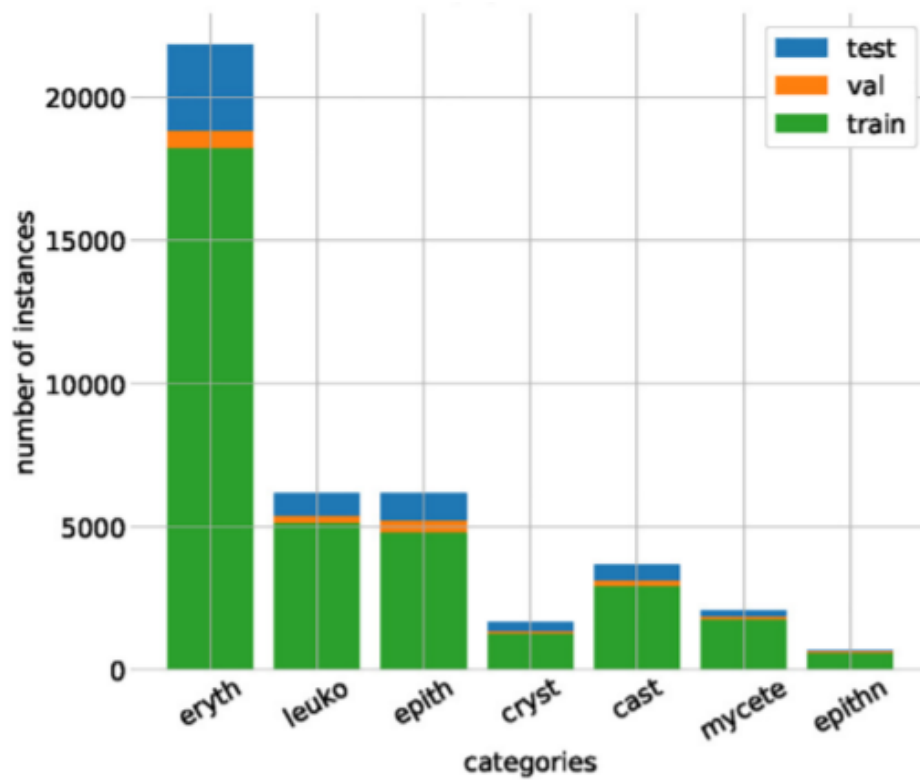
(d) (From [24]))
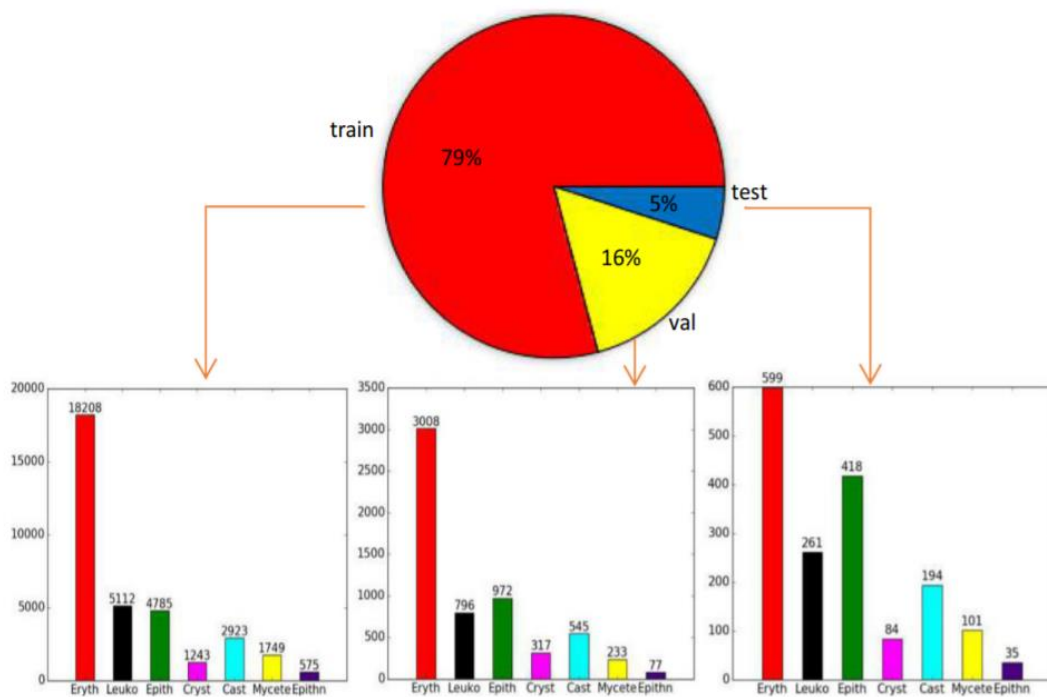
Fig. 5 Dataset organization and categories distribution

(e) (From [38]))

(Fig 15. Exploratory Data Analysis)

Object Detection Method:

Deep Learning-based approaches can perform feature-extraction while simultaneously classifying. Thus, they have demonstrated higher performance in object detection tasks. A Convolutional Neural Network can effectively capture the spatial and temporal dependencies in an image using suitable filters. The convolution operation objective is to extract the high-level features from the input image, such as edges.

For this study, the YOLOv3 object detection method [35, 2016], [36, 2018] was adopted. YOLOv3 (You Only Look Once version 3) is an object detection algorithm for converting RGB image data. It is a one-stage detection algorithm, and it is framed as a regression problem. Instead of selecting only particular parts of an image, it predicts classes and bounding boxes for the whole image.
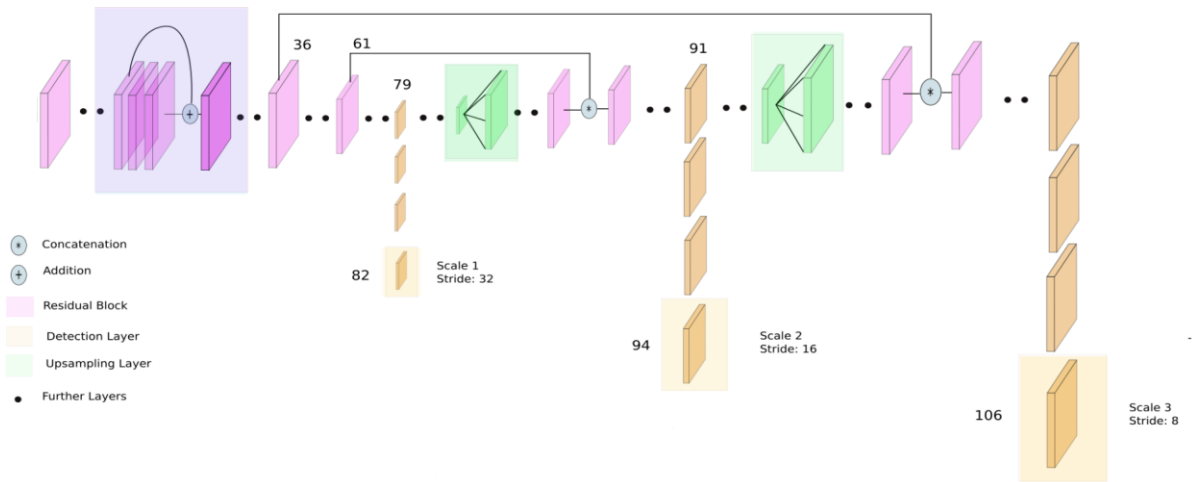
(Fig 16. Network Architecture (From [36]))

The input image is divided into grid cells wherein **only** one object is predicted by each grid cell. However, multiple number of bounding boxes are predicted by each grid cell for every object. A box confidence score is assigned to each of these bounding boxes. This confidence score indicates the likeliness of the box containing an object and the accuracy of the box as well. It also predicts conditional class probabilities that is, the likeliness of an object belonging to a particular class.

$$b_x = \sigma(t_x) + c_x$$
$$b_y = \sigma(t_y) + c_y$$
$$b_w = p_w e^{t_w}$$
$$b_h = p_h e^{t_h}$$
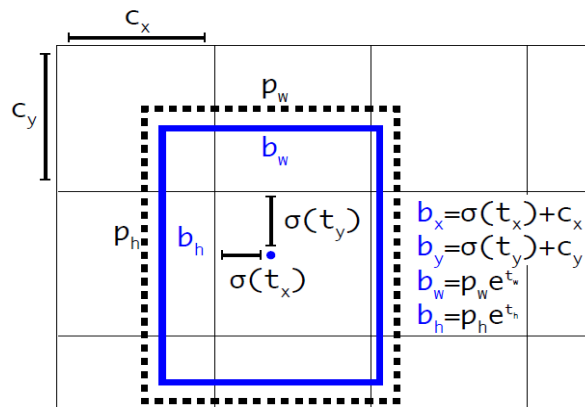
(Fig 17. Bounding Boxes (From [36]))

Only one bounding box out of the many bounding boxes predicted is responsible for the object when computing the loss for the true positive. The bounding box with the highest IoU (intersection over union) annotated on the image is selected.

$$\lambda_{\text{coord}} \sum_{i=0}^{S^2} \sum_{j=0}^{B} \mathbb{1}_{ij}^{\text{obj}} \left[(x_i - \hat{x}_i)^2 + (y_i - \hat{y}_i)^2 \right]$$

$$+ \lambda_{\text{coord}} \sum_{i=0}^{S^2} \sum_{j=0}^{B} \mathbb{1}_{ij}^{\text{obj}} \left[\left(\sqrt{w_i} - \sqrt{\hat{w}_i} \right)^2 + \left(\sqrt{h_i} - \sqrt{\hat{h}_i} \right)^2 \right]$$

$$+ \sum_{i=0}^{S^2} \sum_{j=0}^{B} \mathbb{1}_{ij}^{\text{obj}} \left(C_i - \hat{C}_i \right)^2$$

$$+ \lambda_{\text{noobj}} \sum_{i=0}^{S^2} \sum_{j=0}^{B} \mathbb{1}_{ij}^{\text{noobj}} \left(C_i - \hat{C}_i \right)^2$$

$$+ \sum_{i=0}^{S^2} \mathbb{1}_{i}^{\text{obj}} \sum_{c \in \text{classes}} (p_i(c) - \hat{p}_i(c))^2$$

(Fig 18. IoU mathematics (From [36]))

The classifier is limited to a certain region using region proposal methods. YOLO accesses the whole image in predicting boundaries. It has less false positives in background areas. To compute the likelihood of an input belonging to a certain label, YOLOv3 employs multi-label classification and substitutes the softmax function with independent logistic classifiers. [2018, 36]

The DarkNet-53 neural network framework was adopted as the backbone for YOLOv3. Transfer learning was used so that the weights of the model were initialized with weights from the same architecture pre-trained on the MS COCO dataset [36, 2018]. This approach was adopted as transfer learning helps training of deep neural networks with comparatively little data, accuracy is high, and the training time is reduced. The source code available in [37] was used for implementation.

	Type	Filters	Size	Output
	Convolutional	32	3 × 3	256 × 256
	Convolutional	64	3 × 3 / 2	128 × 128
	Convolutional	32	1 × 1	
1×	Convolutional	64	3 × 3	
	Residual			128 × 128
	Convolutional	128	3 × 3 / 2	64 × 64
	Convolutional	64	1 × 1	
2×	Convolutional	128	3 × 3	
	Residual			64 × 64
	Convolutional	256	3 × 3 / 2	32 × 32
	Convolutional	128	1 × 1	
8×	Convolutional	256	3 × 3	
	Residual			32 × 32
	Convolutional	512	3 × 3 / 2	16 × 16
	Convolutional	256	1 × 1	
8×	Convolutional	512	3 × 3	
	Residual			16 × 16
	Convolutional	1024	3 × 3 / 2	8 × 8
	Convolutional	512	1 × 1	
4×	Convolutional	1024	3 × 3	
	Residual			8 × 8
	Avgpool		Global	
	Connected		1000	
	Softmax			

(Fig 19. DarkNet-53 backbone architecture (From [36]))

The model was trained and tested using Google Colaboratory with an NVIDIA Tesla K80 Graphics Card (4992 Compute Unified Device Architecture (CUDA) cores and 24 GB graphics memory).

```
+-----------------------------------------------------------------------------+
| NVIDIA-SMI 495.44       Driver Version: 460.32.03    CUDA Version: 11.2      |
|-------------------------------+----------------------+----------------------+
| GPU  Name        Persistence-M| Bus-Id        Disp.A | Volatile Uncorr. ECC |
| Fan  Temp  Perf  Pwr:Usage/Cap|         Memory-Usage | GPU-Util  Compute M. |
|                               |                      |               MIG M. |
|===============================+======================+======================|
|   0  Tesla K80           Off  | 00000000:00:04.0 Off |                    0 |
| N/A   37C    P8    29W / 149W |      0MiB / 11441MiB |      0%      Default |
|                               |                      |                  N/A |
+-------------------------------+----------------------+----------------------+

+-----------------------------------------------------------------------------+
| Processes:                                                                  |
|  GPU   GI   CI        PID   Type   Process name                  GPU Memory |
|        ID   ID                                                   Usage      |
|=============================================================================|
|  No running processes found                                                 |
+-----------------------------------------------------------------------------+
```

(Fig 20. GPU specifications)

The number of iterations was set to 14,000 (as specified in [37]). The classes, number of filters, steps, jitter, and other hyperparameters were tuned in the configuration file to customize the model to our requirements. The model was trained on a custom dataset as documented in [37].

The program ran for 10138 iterations. It took 50+ hours for it to train, with 1000 iterations taking about 5 hours even with a GPU that supports fast computation.

Method Assessment:

Precision–recall curves and average precision (AP) indicator were used to evaluate DarkNet YOLOv3's performance [36, 2018]. The Intersection over Union (IoU) was calculated to estimate precision and recall. The area of overlap between the predicted and ground truth bounding boxes is divided by the area of union between them to produce this metric. A correct detection (True Positive, TP) was considered for IoU 0.5, and an incorrect detection (False Positive, FP) for IoU 0.5. When no corresponding ground truth is found, a False Negative (FN) is assigned. Precision (P) and recall (R) are calculated using the formulae below based on the preceding metrics.

True Positive- TP was considered for IoU $\geq$ 0.5

False Positive- FP for IoU < 0.5 (Indicates a wrong detection)

False Negative- FN is assigned when no corresponding ground truth is detected.

Precision (P)= TP / (TP + FP)

Recall (R) = TP / (TP + FN)

The average precision (AP) is estimated by the area under the precision–recall curve.

34

$$\text{box confidence score} \equiv P_r(object) \cdot IoU$$
$$\text{conditional class probability} \equiv P_r(class_i | object)$$
$$\text{class confidence score} \equiv P_r(class_i) \cdot IoU$$
$$= \text{box confidence score} \times \text{conditional class probability}$$

where

$P_r(object)$ is the probability the box contains an object.

IoU is the IoU (intersection over union) between the predicted box and the ground truth.

$P_r(class_i | object)$ is the probability the object belongs to $class_i$ given an object is presence.

$P_r(class_i)$ is the probability the object belongs to $class_i$

(Fig 21. Mathematics behind the metrics of performance assessment (From [35]))

RESULTS of PART 2:

Indicators used while training:

The Mean Average Precision (mAP) was used as the primary indicator to analyze the accuracy of the model. We trained the model while the mAP percentage increased and the loss decreased. The mAP percentage value was calculated during training. The images as part of the validation set were used to calculate the mAP. The loss curves also indicate accuracy, however, mAP is considered to be a better indicator [36, 2018].

Learning results of the object detection method:

At some points in the graph even though the mAP percentage reduces, we still continued training as the recall values were still increasing. [35, 2016]

We adopted 'early-stopping' to prevent overfitting. Also, due to the time it takes to run the program, and because of the desirable mAP value obtained, we stopped training at 10138 iterations. Thus the image data was analyzed effectively by reducing the loss rate on the data and increasing mAP.

The weights file was updated for every 100 iterations. The best weights obtained were saved and can be used for further testing and manhole classification. The weights which gave the best mAP percentage were saved separately in a different file for further use and testing.

Inference results of the object detection method:

The average precision (AP, %) and the mean average precision (mAP, %) values are in the table below. The results in Table 1 display the IoU cutoff at 0.5 (AP50).

Considering the information in the table, it is observed that all of the predictions were not made correctly by DarkNet-53 YOLOv3. However, DarkNet YOLOv3 achieved an IoU value of 64.86% and a mAP of 92.40%.

Class ID	Class Name	True Positive (TP)	False Positive (FP)	Average Precision (AP)
0	cast	3137	686	90.91 %

1	cryst	1555	285	94.66 %
2	epith	5814	1835	91.62 %
3	epithn	617	124	86.11 %
4	eryth	20318	2545	94.14 %
5	leuko	5997	1731	95.65 %
6	mycete	1949	365	93.72 %

Confidence Threshold	TP	FP	FN	Average IoU	Precision	Recall	F1 score	mAP@0.5
0.25	39387	7571	2848	64.86 %	0.84	0.93	0.88	0.924018

Comparing these results with the current state of the art (from [38]):

Backbone + Methods	MAP	eryth	leuko	epith	cryst	cast	mycete	epithn
Resnet50 + Faster R-CNN [30]	73.4	59.1	85.7	80	74.2	61.4	79.5	71.3

Resnet50 + FPN [24]	86.77	94.68	92.62	89.03	83.17	71.11	88.91	87.88
Resnet50 + RetinaNet [24]	84.28	74.33	95.55	85.84	84.73	76.65	87.35	85.53
Resnet101 + SNIPER	80.32	84.62	89.44	80.1	85.67	74.83	80.31	67.3
Resnet50 + BCPNet [38]	88.20	94.85	94.38	87.99	84.66	74.57	90.71	90.21
Darknet-53 + YOLOv3 (this report)	92.40	94.14	95.65	91.62	94.66	90.91	93.72	86.11

Here, the cast detection accuracy is very high though it is the most difficult sediment to detect [39], [40].

Testing:

The model was tested on 6 images that weren't a part of the training or validation set. The weights which contained the best mAP percentage were used for testing the images. The figures below show samples of the images returned after testing by the model.
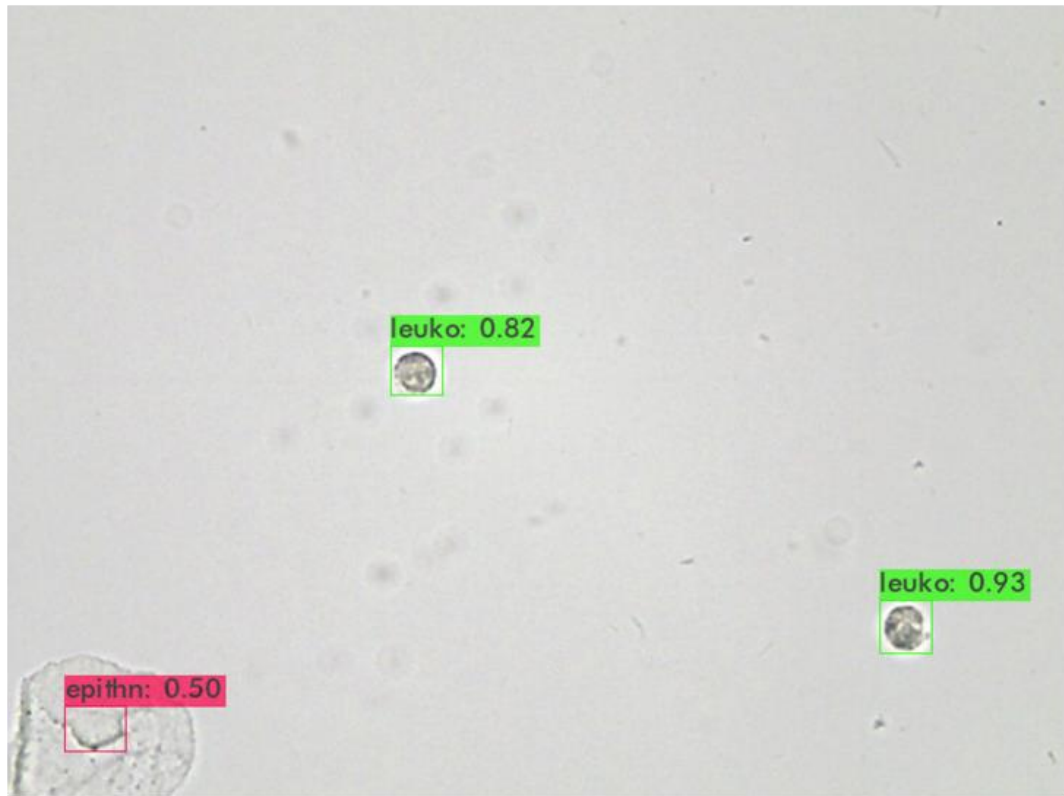
(a)
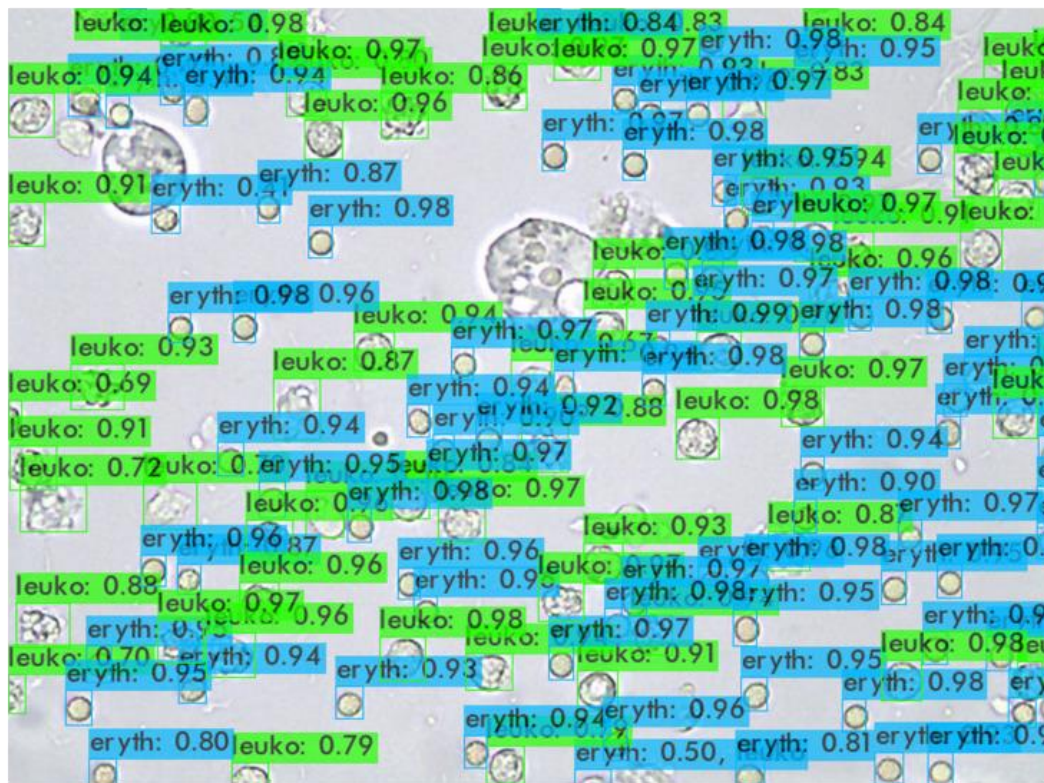
(b)

(Fig 23. Images used for testing the accuracy of the model)

CONCLUSION

Summary:

In this project, the spectrophotometric colorimetric detection method for nitrite is adopted using the Griess test in a microfluidic environment. The modeling and simulation of this sensor is done using COMSOL multiphysics software.

In addition, transfer learning using pre-existing object detection based Convolutional Neural Networks is adopted to detect and classify urine sediment. This is done using Python and Google Colaboratory.

Future Scope:

As in [10, 1978], there is a relationship between the quantity of nitrite in urine samples and UTI but further research has to be conducted to model the relationship. In [3], the relationship between the number of E.coli bacteria and concentration of nitrite in the urine sample was modelled as a linear relationship. Thus, it was hypothesized in [3] that in such cases, the urine culture test could be avoided.

In cases wherein the urine culture test is mandatory to provide valuable information on the detection of the type of bacterial UTI, a microfluidic lab on chip system could be detected for speedy test results as compared to the current 24 – 72 hours time range. Further research can also be done to understand and model the relationship between the quantity of nitrite and the type of bacteria.

Integrating this device with an IoT enabled automated platform would help commercialize this microfluidic sensor. Once it is used in hospitals, further research can also be done to understand the relationship between the quantity of nitrite and the type of bacteria. Some bacteria may convert less nitrate to nitrite and so may convert higher quantities. This can then be used to eliminate the Urine Culture Test or definitely reduce the time period as the possibilities for the type of bacteria can be narrowed down.

The microscopic analysis system can also be improved by using the above model for real time detection and classification of microscopic urine images.

REFERENCES

1. Mach, K. E., Wong, P. K., & Liao, J. C. (2011). *Biosensor diagnosis of urinary tract infections: a path to better treatment? Trends in Pharmacological Sciences, 32(6), 330–336.* doi:10.1016/j.tips.2011.03.001

2. Thakre, S. S. (2012). *Can the Griess Nitrite Test and a Urinary Pus Cell Count of ≥5 Cells Per Micro Litre of Urine in Pregnant Women be Used for the Screening or the Early Detection of Urinary Tract Infections in Rural India? JOURNAL of CLINICAL AND DIAGNOSTIC RESEARCH.* doi:10.7860/jcdr/2012/4565.2547

3. Feng, S., Roseng, L. E., & Dong, T. (2015). *Quantitative detection of Escherichia coli and measurement of urinary tract infection diagnosis possibility by use of a portable, handheld sensor. 2015 IEEE International Symposium on Medical Measurements and Applications (MeMeA) Proceedings.* doi:10.1109/memea.2015.7145271

4. Pal, A., Kulkarni, M. B., Gupta, H., Ponnalagu, R. N., Dubey, S. K., & Goel, S. (2021). *Portable and Autonomous Device for Real-time Colorimetric Detection: Validation for Phosphorous and Nitrite Detection. Sensors and Actuators A: Physical, 330, 112896.* doi:10.1016/j.sna.2021.112896

5. S. Dudala, S. K. Dubey and S. Goel, "Fully Integrated, Automated, and Smartphone Enabled Point-of-Source Portable Platform With Microfluidic Device for Nitrite Detection," in IEEE Transactions on Biomedical Circuits and Systems, vol. 13, no. 6, pp. 1518-1524, Dec. 2019, doi: 10.1109/TBCAS.2019.2939658.

6. T. Klymkovych, N. Bokla and O. Matviykiv, "Microfluidic Lab-Chip Device Dedicated for Colorimetric Detection of Hazardous Impurities in Water Samples," 2019 IEEE XVth International Conference on the Perspective Technologies and Methods in MEMS Design (MEMSTECH), 2019, pp. 96-100, doi: 10.1109/MEMSTECH.2019.8817402.

7. Reches, M., Mirica, K. A., Dasgupta, R., Dickey, M. D., Butte, M. J., & Whitesides, G. M. (2010). *Thread as a Matrix for Biomedical Assays. ACS Applied Materials & Interfaces, 2(6), 1722–1728.* doi:10.1021/am1002266

8. Mach, K. E., Wong, P. K., & Liao, J. C. (2011). *Biosensor diagnosis of urinary tract infections: a path to better treatment? Trends in Pharmacological Sciences, 32(6), 330–336.* doi:10.1016/j.tips.2011.03.001

9. https://www.mayoclinic.org/tests-procedures/urinalysis/about/pac-20384907

10. Gordon P. James, Ph.D., Kala L Paul, M.D., John B. Fuller, M.D., Urinary Nitrite and Urinary-tract Infection, *American Journal of Clinical Pathology*, Volume 70, Issue 4, 1 October 1978, Pages 671–678, https://doi.org/10.1093/ajcp/70.4.671

11. Flores-Mireles, A., Walker, J., Caparon, M. *et al.* Urinary tract infections: epidemiology, mechanisms of infection and treatment options. *Nat Rev Microbiol* **13,** 269–284 (2015). https://doi.org/10.1038/nrmicro3432

12. Dudala, S., Dubey, S. K., & Goel, S. (2020). *Microfluidic Soil Nutrient Detection System: Integrating Nitrite, pH and Electrical Conductivity Detection. IEEE Sensors Journal, 1– 1.* doi:10.1109/jsen.2020.2964174

13. Q.-H. Wang et al., "Methods for the detection and determination of nitrite and nitrate: A review," Talanta, vol. 165, pp. 709–720, Apr. 2017.

14. Y. Wang and J. D. Holladay, Microreactor Technology and Process Intensification. ACS Publications, 2005.

[15] G. M. Greenway, S. J. Haswell, and P. H. Petsul, "Characterisation of a micro-total analytical system for the determination of nitrite with spectrophotometric detection," Analytica Chimica Acta, vol. 387, no. 1, pp. 1–10, 1999.

[16] V. J. Sieben, C. F. A. Floquet, I. R. G. Ogilvie, M. C. Mowlem, and H.Morgan, "Microfluidic colourimetric chemical analysis system: Application to nitrite detection," Anal. Methods, vol. 2, no. 5, pp. 484–491, 2010.

[17] Pal, A., Amreen, K., Dubey, S. K., & Goel, S. (2021). *Highly Sensitive and Interference-Free Electrochemical Nitrite Detection in a 3D Printed Miniaturized Device. IEEE Transactions on NanoBioscience, 20(2), 175–182.* doi:10.1109/tnb.2021.3063730

[18] M. F. Khanfar, W. Al-Faqheri, and A. Al-Halhouli, "Low cost lab on chip for the colorimetric detection of nitrate in mineral water products," Sensors (Basel), vol. 17, no. 10, Oct. 2017, Art. no. E2345.

19. Deville, W.L. et al. (2004) The urine dipstick test useful to rule out infections A meta-analysis of the accuracy. BMC Urol. 4, 4

20. Jolkkonen, S. et al. (2010) Screening of urine samples by flow cytometry reduces the need for culture. J. Clin. Microbiol. 48, 3117–3121

21. Pieretti, B. et al. (2010) Diagnosis of bacteriuria and leukocyturia by automated flow cytometry compared with urine culture. J. Clin. Microbiol. 48, 3990–3996

22. J. J. Tsai, J. Y. Yeun, V. A. Kumar, and B. R. Don, "Comparison and interpretation of urinalysis performed by a nephrologist versus a hospital-based clinical laboratory," American journal of kidney diseases, vol, 46, pp. 820–829, 2005.

23. Detection and Classification of RBCs and WBCs in Urine Analysis with Deep Network Xingguo Zhang, Guoyue Chen, Kazuki Saruta and Yuki Terata Faculty of Systems Science and Technology- ACHI 2018 : The Eleventh International Conference on Advances in Computer-Human Interactions

24. Liang, Y., Tang, Z., Yan, M., & Liu, J. (2018). *Object detection based on deep learning for urine sediment examination. Biocybernetics and Biomedical Engineering, 38(3), 661–670.* doi:10.1016/j.bbe.2018.05.004

25. https://github.com/dipamgoswami/UMID-Urine-Microscopic-Image-Dataset

26. Vicenzo Abichequer, Felipe Lammel, Marcio Pinho, and Isabel Manssour. 2017. An automatic method for identification of cystine crystals in urine sediment. In Proceedings of the Symposium on Applied Computing (SAC '17). Association for Computing Machinery, New York, NY, USA, 170–173. DOI:https://doi.org/10.1145/3019612.3028253

27. Li, Q., Yu, Z., Qi, S., He, Z., Li, S., & Guan, H. (2020). *Inspection of visible components in urine based on deep learning. Medical Physics.* doi:10.1002/mp.14118

28. Burton, R. J., Albur, M., Eberl, M., & Cuff, S. M. (2019). *Using artificial intelligence to reduce diagnostic workload without compromising detection of urinary tract infections. BMC Medical Informatics and Decision Making, 19(1).* doi:10.1186/s12911-019-0878-9

29. Q. Ji, X. Li, Z. Qu and C. Dai, "Research on Urine Sediment Images Recognition Based on Deep Learning," in IEEE Access, vol. 7, pp. 166711-166720, 2019, doi: 10.1109/ACCESS.2019.2953775.

30. Liang, Y., Kang, R., Lian, C. *et al.* An End-to-End System for Automatic Urinary Particle Recognition with Convolutional Neural Network. *J Med Syst* **42,** 165 (2018). https://doi.org/10.1007/s10916-018-1014-6

31. Liao, J.C. et al. (2006) Use of electrochemical DNA biosensors for rapid molecular identification of uropathogens in clinical urine specimens. J. Clin. Microbiol. 44, 561–570

32. Liao, J.C. et al. (2007) Development of an advanced electrochemical DNA biosensor for bacterial pathogen detection. J. Mol. Diagn. 9, 158– 168

33. Mach, K.E. et al. (2009) Multiplex pathogen identification for polymicrobial urinary tract infections using biosensor technology: a prospective clinical study. J. Urol. 182, 2735–2741

34. Mach, K.E. et al. (2011) A biosensor platform for rapid antimicrobial susceptibility testing driectly from clinical samples. J. Urol. 185, 148– 153

35. Redmon, J.; Divvala, S.; Girshick, R.; Farhadi, A. You Only Look Once: Unified, Real-Time Object Detection. In Proceedings of the Computer Vision and Pattern Recognition, Las Vegas, NV, USA, 27–30 June2016; pp. 779–788.

36. Redmon, J., & Farhadi, A. (2018). Yolov3: An incremental improvement. *arXiv preprint arXiv:1804.02767.*

37. https://github.com/AlexeyAB/darknet

38. M. Yan, Q. Liu, Z. Yin, D. Wang and Y. Liang, "A Bidirectional Context Propagation Network for Urine Sediment Particle Detection in Microscopic Images," ICASSP 2020 - 2020 IEEE International Conference on Acoustics, Speech and Signal Processing (ICASSP), 2020, pp. 981-985, doi: 10.1109/ICASSP40776.2020.9054367.

39. Budak YU, Huysal K. Comparison of three automated systems for urine chemistry and sediment analysis in routine laboratory practice. Clin Lab. 2011;57(1-2):47-52. PMID: 21391464.

40. M. Yan, Q. Liu, Z. Yin, D. Wang and Y. Liang, "A Bidirectional Context Propagation Network for Urine Sediment Particle Detection in Microscopic Images," ICASSP 2020 - 2020 IEEE International Conference on Acoustics, Speech and Signal Processing (ICASSP), 2020, pp. 981-985, doi: 10.1109/ICASSP40776.2020.9054367.

41. V. Hessel, H. Löwe, and F. Schönfeld, "Micromixers—a review on passive and active mixing principles," Chem. Eng. Sci., vol. 60, no. 8, pp. 2479–2501, 2005.

42. D. Gobby, P. Angeli, and A. Gavriilidis, "Mixing characteristics of T-type microfluidic mixers," J. Micromechanics Microeng., vol. 11, no. 2, pp. 126–132, 2001.

43. Banerjee, T., Ghoshal, S. & Bhattacharya, B.B. COMSOL-Based Design and Validation of Dilution Algorithm with Continuous-Flow Lab-on-Chip. *INAE Lett* **2,** 55–63 (2017). https://doi.org/10.1007/s41403-017-0022-z

44. Tiwari, S.K., Bhat, S. & Mahato, K.K. Design and Fabrication of Low-cost Microfluidic Channel for Biomedical Application. *Sci Rep* **10,** 9215 (2020). https://doi.org/10.1038/s41598-020-65995-x

45. Howard AS (2007) Introduction to fluid dynamics for microfluidic flows. In: Lee H, Ham D, Westervelt RM (eds) CMOS biotechnology. Springer, New York, pp 5–30

46. Váradi, L., Breedon, M., Chen, F. F., Trinchi, A., Cole, I. S., & Wei, G. (2019). *Evaluation of novel Griess-reagent candidates for nitrite sensing in aqueous media identified via molecular fingerprint searching. RSC Advances, 9(7), 3994–4000.* doi:10.1039/c8ra07656a

47. H.N. Wilson, Absorptiometry and 'colorimetric analysis', Approach Chem. Anal. (1966) 222–259, http://dx.doi.org/10.1016/b978-0-08-011543-6.50016- 3.

48. P.K. Dasgupta, I.Y. Eom, K.J. Morris, J. Li, Light emitting diode-based detectors: absorbance, fluorescence and spectroelectrochemical measurements in a planar flow-through cell, Anal. Chim. Acta 500 (1–2) (2003) 337–364, http:// dx.doi.org/10.1016/S0003-2670(03)00575-0.

49. P. Yeh, N. Yeh, C.H. Lee, T.J. Ding, Applications of LEDs in optical sensors and chemical sensing device for detection of biochemicals, heavy metals, and environmental nutrients, Renew. Sustain. Energy Rev. 75 (November) (2017) 461–468, http://dx.doi.org/10.1016/j.rser.2016.11.011.

50. Kim, T.H., Lee, J.M., Chung, B.H. *et al.* Development of microfluidic LED sensor platform. *Nano Convergence* **2,** 12 (2015). https://doi.org/10.1186/s40580-015-0043-9